~~Satellite-based evidence of regional~~ Regional and seasonal ~~Arctic cooling~~ changes in solar spectral reflectance and in radiative forcing by brighter and ~~wetter~~ liquid water clouds in the Arctic from satellite remote sensing

Luca Lelli[1,2,4], Marco Vountas[1], Narges Khosravi[3,5], and John P. Burrows[1]

[1]Institute of Environmental Physics and Remote Sensing, University of Bremen, Germany
[2]NASA Goddard Space Flight Center, Greenbelt, MD, USA
[3]Alfred-Wegener-Institut, Bremerhaven, Germany
[4]now at Institute of Remote Sensing Methods, German Aerospace Agency (DLR), Wessling, Germany
[5]now at EUMETSAT, Darmstadt, Germany

Correspondence: Luca Lelli (luca@iup.physik.uni-bremen.de, luca.lelli@dlr.de)

Abstract. ~~Using two decades of satellite-based measurements of~~ Two decades of measurements of spectral reflectance of solar radiation at the ~~top-of-atmosphere~~ top of atmosphere and a complementary record of cloud properties ~~, it is concluded that the loss of Arctic brightnessdue to sea ice retreat~~ from satellite passive remote sensing have been analysed for their pan-Arctic, regional and seasonal changes. The pan-Arctic loss of brightness, explained by the retreat of sea ice during the current warming period, is not compensated by a ~~pan-Arctic increase in cloudiness, but rather by a~~ corresponding increase in cloud cover. A systematic change in the thermodynamic phase of ~~cloud and a resultant effect on cloud reflectance. Liquid water content of the clouds has increased~~clouds took place, shifting towards the liquid phase at the expense of the ice phase. Without significantly changing the total cloud optical thickness or the mass of condensed water in the atmosphere, liquid water content has increased, resulting in positive trends in ~~susceptible cloud properties. Consequently,~~ liquid cloud optical thickness and albedo. This leads to a cooling trend by clouds ~~is~~ being superimposed on top of the pan-Arctic amplified warming, induced by the anthropogenic release of greenhouse gases, the ice albedo feedback and related effects. Except above the permanent and parts of the marginal sea ice zone around the Arctic circle, the rate of surface cooling by clouds has increased, both in spring (-32% in total radiative forcing for the whole Arctic) and in summer (-14%). The magnitude of this effect depends on both the underlying surface type and changes in the regional Arctic climate.

1 Introduction

~~The most recent climate projections indicate that the Arctic will be free of sea ice by the summer of 2035 (Guarino et al., 2020). The Arctic near-surface increase of temperatures is about twice the global average over the past four decades. This is referred to as "Arctic Amplification" (Serreze and Francis, 2006). The~~ The size of a temperature increase from a doubling of the ~~carbon dioxide atmospheric loading~~ column of carbon dioxide, CO_2, in the atmosphere was first quantified by Svante Arrhenius in 1896 (Arrhenius, 1896). ~~The~~ This was a remarkable achievement and ahead of his time given the lack of reliable atmospheric measurements of greenhouse gases (for more details see Rodhe et al., 1997, and references therein). The first routine monitoring of CO_2 fraction in dry air was initiated by Charles Keeling at the Mauna Loa Observatory only in 1957 (Keeling, 1958, 1960; Keeling et al., 1976). This led eventually to the recognition of the impact of the anthropogenic release of greenhouse gases on the ~~surface temperature~~ global surface temperature, which has become an increasingly important topic of scientific interest, ~~pubic~~ public debate and concern and international environmental policy, since at least 1990. However, the Arctic is a special case (Serreze and Barry, 2011).

The Arctic near-surface increase of temperatures is about twice that of the global average during the past four decades (Södergren and McDonald, 2022). This phenomenon is referred to as "Arctic Amplification" (Serreze and Francis, 2006). As a consequence, the most recent climate projections indicate that the Arctic may be free of sea ice by the summer of 2035 (Guarino et al., 2020). Even if global temperatures are held to the target of a 2 °C increase, the Arctic sea ice is projected to disappear (i.e. sea ice extent < 1 million km^2) in September between 2035 and 2038 by the majority of the models in the Climate Model Intercomparison Project Phase 6 (CMIP6, Notz and Community (2020)).

Clouds play an important role in determining the climate of the Arctic. Modeling the changing behavior of clouds sufficiently accurately is identified as the most uncertain factor in the climate projections of greenhouse gas forcing (Zelinka et al., 2020). This is particularly the case in the Arctic, where the modulation of radiation by clouds in ~~large part because clouds modulate the Arcticradiation budget in~~ the shortwave (SW) and longwave (LW) ~~. .~~ spectral regions is not adequately simulated by state-of-the-art models. Changes in the temperature, water vapor and the availability of ~~cloud condensation nuclei result in turn in changes in the cloud absorption and reflectance. Thus~~condensation nuclei of liquid and ice cloud particles result in changes of scattering and absorption of both SW and LW radiation. Consequently, improved knowledge of the ~~changing~~ changes in optical and radiative properties of ~~clouds,~~ the Earth's surface and the ~~resultant SW reflection and LW emission at the top of the atmosphere are essential~~ clouds are needed to test and thereby improve the accuracy of climate model projections. ~~The most complex and~~

To address these objectives, ambitious measurement endeavours (Wendisch et al., 2019; Shupe et al., 2021) ~~, exploiting the synergy of~~ have exploited the synergistic use of measurements by on-ground, ship and airborne ~~techniques, rely on complementary measurements of satellite sensors which~~ sensors. However, another complementary source of knowledge are measurements by satellite sensors that provide synoptic coverage of the Arctic clouds over long time scales.

Instruments aboard satellites measure the solar radiation scattered back to space from the Arctic surface and atmosphere constituents~~(i.e.~~, such as ice, snow, ocean, land, clouds, trace gases and aerosols (Kokhanovsky and Tomasi, 2020; Serreze and Barry, 2014)~~). Each contribution~~. Each constituent has a different response to radiation depending on ~~their~~ its physical properties. Incoming solar SW radiation in the ultraviolet and visible is scattered strongly by ice, snow, and clouds, whereas open ~~waters absorb~~ water absorbs significantly and scatter back to space much less electromagnetic radiation in the solar spectral range. On the other hand, LW radiation fluxes are also modulated by clouds, which may warm or cool both the Top-Of-Atmosphere (TOA) and the surface. The changes at the surface ~~resulting~~ result from the interplay ~~of~~ between changes in sea ice~~properties~~, snow and cloud properties~~in the atmosphere~~. This lead to a nonlinear response of the radiation budget in the Arctic to changes in temperature (Lindsay and Zhang, 2005).

Cloud fractional cover (CFC) ~~over the Arctic can~~ is the primary parameter modulating radiation. In the Arctic, CFC may be as large 70% throughout the year (Karlsson and Devasthale, 2018). The measured magnitude and variability of CFC depends on ~~atmospheric conditions, which impact on~~ meteorological conditions, including cloud nucleation and growth ~~, and~~ rates. Currently our knowledge of CFC also depends on the type of sensors ~~used to measure it~~ and assumptions used in its retrieval (Chan and Comiso, 2013). The CFC ~~seasonal cycle exhibits a strong bimodal distribution, with a maximum up to~~ annual cycle in the Arctic has two maxima. One occurs in summer, where CFC may be as large as 90% ~~in summer along~~ and is located in the North Atlantic ~~throughout~~ and the circumpolar ocean waters~~and a minimum of~~. The second maximum of CFC, which is approximately 40%~~in~~, occurs during the winter months (Eastman and Warren, 2010b, a; Boccolari and Parmiggiani, 2018). Rather than having a latitudinal dependence, CFC in the Arctic appears to be dependent on the underlying surface type, meteorology and topography. Distinct patterns~~having divergent CFC trends and types in the Arctic~~, having different signs and magnitudes of the CFC trends, have been identified in the Arctic, which follow the contour between sea ice and open ~~waters contours. Using~~ water. However, using the same data sets does not guarantee ~~consistent~~ that there is agreement between analysis and interpretation of the ~~observations. This is the case for Boccolari and Parmiggiani (2018), where~~ same observations by different authors. For example, the study of Boccolari and Parmiggiani (2018), in which CFC data, derived from observations of AVHRR (see Tab. A1 for the meaning of all technical acronyms) over the Arctic between 1982 and 2009, ~~is in unexpected and large disagreement~~ disagrees unexpectedly with results from Schweiger (2004) and Wang and Key (2005b), even though all three research groups use the same data.

Clouds ~~are the most important atmospheric factor in the modulation of energy flow exchange between~~ modify the SW and LW energy flows at local scale. However, the distribution of clouds is influenced by large scale circulation patterns connecting the Arctic and its surroundings. Sledd and L'Ecuyer (2019) ~~partitions~~ separates the relative importance of ~~surface and atmosphere with respect~~ the surface and the atmosphere to the changes of albedo at TOA. While the majority of the variability is ~~controlled~~ determined by surface reflection, TOA albedos are consistently influenced by radiative transfer in the atmosphere: the contribution of the atmospheric reflection being approximately 84% of the total Arctic albedo. This finding is ~~relevant for~~ important when interpreting the behaviour of a melting cryosphere, in which the ~~relative~~ changes in surface reflection are offset by atmospheric reflection~~, primarily~~. The latter, although wavelength dependent, is dominated by the reflectance of clouds (Donohoe and Battisti, 2011). Consequently and as expected, the presence of clouds ~~limits~~ reduces the impact of the changes of the surface reflectance on the ~~spectral reflectance at TOA (R_λ^{TOA})~~albedo at TOA (Sledd and L'Ecuyer, 2021a). Hence, a decrease in summer CFC over Greenland is held responsible for the ~~ice mass loss acceleration~~ acceleration of the loss of ice mass and, consequently, ~~for the decrease in albedo~~ a decrease of the albedo and spectral reflectance at TOA (R_λ^{TOA}). A decrease in cloudiness implies an increase of SW downwelling fluxes at the surface. This pattern is correlated with the ~~synoptic~~ North Atlantic Oscillation (Hofer et al., 2017) and anticyclonic activity promoting adiabatic tropospheric warming of subsiding air masses (Shahi et al., 2020). These results indicate that Arctic cloudiness is not only dependent on the underlying surface, but is also affected by synoptic scale meteorological processes.

In Pistone et al. (2014), a downward trend of all-sky albedo across the Arctic is reported. This is not compensated by an opposite trend in cloudiness, thus ~~levelling out~~ a levelling of the recent pan-Arctic reflectance trend. However, this analysis is limited to oceanic regions and additional uncertainties are caused by the conversion from clear-sky to all-sky albedo at the beginning of their record. As the clear-sky signal is derived from the ~~sea-ice~~ sea ice record with sensors for which the atmosphere is almost entirely transparent, the all-sky albedo is computed with a post-hoc method adding the atmospheric part and is not the outcome of direct satellite measurements. ~~He et al. (2019) reports significant regional covariance of CFC and sea ice. Strong negative correlations are seen over Beaufort and East Siberian Seas. The highest CFC occurs typically over marginal sea ice regions. The latter is negatively correlated with sea ice anomalies. The~~

He et al. (2019) reports that the magnitude of the ~~surface~~ Arctic ice albedo feedback is ~~limited by the formation of low-level cloudsfrom the evaporation of~~ locally dampened by clouds. Although a CFC increase is detected over some areas of frozen surface, only the negative correlations between clouds and retreating sea ice are statistically significant. This implies that over the ~~melted sea ice regions. In such conditions, clouds have a negative feedback, in the SW radiation spectral region. This offsets LW radiation emission. Overall, He et al. (2019) consider that CFC over the melted water influences the albedo change in the albedo feedback process. The extra CFC resulting from sea ice loss is a second-order contribution~~marginal sea ice zones of transitional albedo (e.g. of the Beaufort Sea throughout the Laptev Sea) enhanced cloud cover effectively compensates the decrease of Arctic albedo at TOA, arising from the loss of sea ice.

The feedback mechanisms associated with the increase in surface absorption of solar radiation are ~~often cited as the main contributor to the loss~~ cited as providing an important contribution to the warming and then melting of ice and snow in the Arctic ~~(Serreze and Francis, 2006; Crook et al., 2011)~~(Serreze and Francis, 2006; Crook et al., 2011; Sledd and L'Ecuyer, 2021a) . However, Pithan and Mauritsen (2014) ~~proposes~~ propose that temperature-related processes dominate the Arctic warming. For example, with the increase of Arctic temperatures, the thermodynamic equilibrium between water vapor, liquid water and ice is altered, which imbalances the phase of clouds in presence of aerosol particles (cloud condensation nuclei - CCN - or ice nucleating particles - INP). Dependent on the cloud phase, the particle radius changes: liquid droplets being typically smaller than ice crystals (Mioche et al., 2017). This in turn affects the average optical thickness of clouds. The liquid and ice phases in the clouds interact differently with radiation in the solar and in the terrestrial spectral range. Already early studies (Curry et al., 1996) stressed that the additional presence of an underlying cold, bright surface and frequent temperature inversions impact atmospheric radiation budget through processes involving water condensate in form of liquid and ice clouds as a function of temperature profile. In a warming Arctic, it is expected that clouds will increase their liquid water content and thus reflect more SW radiation (Boisvert and Stroeve, 2015; Ceppi et al., 2016; Cesana and Storelvmo, 2017). Temperature rise influences cloud formation and precipitation (Herman and Goody, 1976; Curry et al., 1996)~~, which~~ . This might amplify warming in the Arctic region (Taylor et al., 2013), although there are disagreements ~~on~~ about the impact of clouds in this respect. For ~~instance~~ example, Screen and Simmonds (2010) reported that changes in CFC do not strongly contribute to the Arctic Amplification despite their role in "enhanced warming in the lower part of the atmosphere during summer and early autumn", whereas Francis and Hunter (2006) relate the loss rate of the ~~the~~ perennial sea ice edge shelves to CFC and the downwelling LW during spring months.

In addition to the warming from the ~~release~~ increased concentration of greenhouse gases ~~,~~ and sea ice albedo feedback, changes in the dynamics of air masses and physical properties of clouds ~~may contribute to the tropospheric thermal emission.~~

~~CFC aside~~influence the flow in energy into the Arctic. Ignoring any change in CFC, the optical properties of clouds, such as the optical thickness (COT, τ) and effective radius $\mathrm{r_{eff}}$ of droplets/crystals, and liquid/ice water ~~content~~ path (LWP/IWP), regulate ~~downwelling LW~~both the downwelling and upwelling LW radiation. Model projections ~~of the century ahead~~ show that Arctic clouds during summer are ~~rather unaffected~~ weakly influenced by sea ice variability~~but~~. However, their response to sea ice loss is to become optically thicker, to have higher LWP, and ~~more frequent low-level~~ to be more frequently in the liquid phase within the Arctic boundary layer (Morrison et al., 2019). ~~Hence~~In summary, the changes in τ and thermodynamic phase of clouds enhance or suppress cloud radiative forcing (CRF) at the surface. This ~~behavior~~ behaviour has been identified in the continuous surface measurements above the Beaufort and Chuckchi Seas (Shupe and Intrieri, 2004), at Ny-Ålesund, Svalbard (Ebell et al., 2019) and in the data products retrieved from AVHRR (Francis and Hunter, 2006).

From the above review of ~~current knowledge about~~ our current knowledge of the changing conditions in the Arctic, we ~~consider~~ conclude that investigations of the R_λ^{TOA} and the cloud properties over the past two decades ~~will provide~~ provides valuable insight into the evolution of the Arctic ~~Amplification. We~~ climate. To achieve this goal, we have prepared a consolidated R_λ^{TOA} data set from 1995 to ~~2018. A key set of satellite sensors record backscattered radiation in the solar portion of the spectrum. Consequently~~2018 (https://doi.pangaea.de/10.1594/PANGAEA.933905). This data set from satellite sensors comprises backscattered radiation at TOA in the SW solar spectral range. Thus, this study focuses on the months between April and September. The Arctic seasons considered are spring, defined for our purposes as April May June (AMJ) and summer, July August September (JAS)~~(see App. 2.1).~~. The investigation of R_λ^{TOA} ~~trends involved analysis of the last~~ involved the determination of trends of twenty years of cloud properties from the observations of AVHRR, retrieved with the ~~latest algorithms (Stengel et al., 2020)(see App. 2.2), which~~ most recent algorithms (Stengel et al., 2020). They supersede older popular data sets, for which specific errors have been found (Zygmuntowska et al., 2012). We build on the heritage of the earlier studies describing the Arctic state and extend the trend analyses limited previously to 1982–1999 ~~(Wang and Key, 2005b, 2003)~~ (Wang and Key, 2003, 2005b).

The objectives of this paper are ~~threefold~~fourfold. Firstly, we provide evidence that space-borne measured ~~,~~ spectral R_λ^{TOA} is a valuable indicator of the changing atmospheric composition and surface properties of the Arctic. Secondly, we determine R_λ^{TOA} trends at regional and seasonal scales and ~~reveal~~ identify unexpected patterns of ~~behavior~~behaviour. Thirdly, we attribute the trends in R_λ^{TOA} above clouds to changes in the thermodynamic phase of clouds. Lastly, we quantify the average ~~radiative forcing by clouds~~ cloud radiative forcing and its changes. We relate the latter to the changes in the physical properties of clouds in response to climate change.

2 Data and Methods

The study of the Arctic ~~geophysical domains~~ by remote sensing requires sensors ~~with~~ having broad spectral coverage ~~at an adequate~~ and sufficient spectral resolution to ~~be able to separate different~~ separate the spectral features of gases, surfaces, liquid water and ice/snow. We define the spectral reflectance measured at TOA - R_λ^{TOA} - ~~as~~ to be

$$R_\lambda^{\mathrm{TOA}} = \frac{\pi\, I_\lambda}{\cos(\theta_0)\, E_\lambda^0}, \tag{1}$$

where I_λ is the Earthshine, i.e. the upwelling scalar radiance measured at TOA (units of photons $\times$ s^{-1} cm^{-2} nm^{-1} sr^{-1}), E_λ^0 the unpolarized downwelling solar irradiance (photons $\times$ s^{-1} cm^{-2} nm^{-1}) and θ_0 the solar zenith angle in degrees.

~~Relevant parameters~~ Parameters of relevance for the R_λ^{TOA} analysis are shown in Fig. 1. The ~~left~~ y-axis on the left of Fig. 1-a shows I_λ, E_λ^0 for a GOME measurement above the Kara Sea, ~~while the right~~ whereas the y-axis ~~shows modeled~~ on the right side shows modelled R_λ^{TOA}, in satellite perspective, representing the TOA signal for typical Arctic geophysical conditions. Fig. 1-b shows the wavelength dependence, at the GOME spectral resolution, of the spectral reflectance for different surface types. The almost flat Earthshine between ~~450–800~~ 450 and 800 nm reveals the presence of a cloud deck or snow surface in the satellite field of view. Ten wavelength bands of spectral width 5-10 nm have been selected satisfying the following requirements: i) they are chosen to be similar to those of ~~sensors'~~ sensor channels used in the literature for comparative purposes~~. Their~~ ; ii) their coverage from the UV to the NIR ~~shall provide differential sensitivity to individual components~~ provides differential sensitivity for the atmospheric constituents and surface types of the Arctic atmosphere-surface~~. Additionally, they should exclude~~ ; iii) they exclude spectral regions of strong absorption by atmospheric trace gases to avoid misinterpretation of the observed ~~behavior~~behaviour. Two exceptions are the spectral regions of the broadband O_3 Chappuis band (525–675 nm) and the narrow O_2 A-band (centred at 760 nm). The former, even if smoothed at 5-10 nm resolution, ~~has information on~~ still contains information about the total column of ozone and ~~on~~ the structure of the upper troposphere and lower stratosphere. Well-mixed ~~gas~~gases, such as oxygen, provide valuable diagnostics about the depth of the atmospheric column, as seen from space. The A-band is used to assess the surface topography in a cloud-free atmosphere (van Diedenhoven et al., 2005) and altitude, geometrical and optical depth of clouds over dark (Rozanov and Kokhanovsky, 2004; Lelli et al., 2012, 2014) and bright (Schlundt et al., 2013) surfaces.

2.1 Reflectance data at TOA

To detect changes on daily, monthly, seasonal and decadal scales several measurements per day ~~of~~ at an adequate spatial resolution must be made over several decades. The polar-orbiting spectrometer suite comprising GOME, SCIAMACHY and GOME-2 (Tab. A2 for their specifications) ~~is an optimal choice~~make measurements of R_λ^{TOA} at the same solar zenith angle and at several times per day as a result of their swath widths. They are a suitable choice, given the individual length of the time series and their high spectral resolution, for the creation of the R_λ^{TOA} time series. Description of GOME can be found in Burrows et al. (1999), while SCIAMACHY and GOME-2 are respectively ~~provided~~ described in Burrows et al. (1995) and ~~?~~ Munro et al. (2016). The detailed steps to harmonize R_λ^{TOA} measured by sensors of different technical specifications are given in the App. A.

~~Sensors measuring~~ While the measurement of solar radiation scattered back to the ~~top of the atmosphere do not measure at night. Measurements in~~ TOA by GOME, SCIAMACHY or GOME-2 takes place only during daylight, radiation in the thermal infrared ($\lambda \gtrsim 4\,\mu$m)~~are~~ , required to record the thermal emission from the surface and the atmosphere~~. In practice,~~

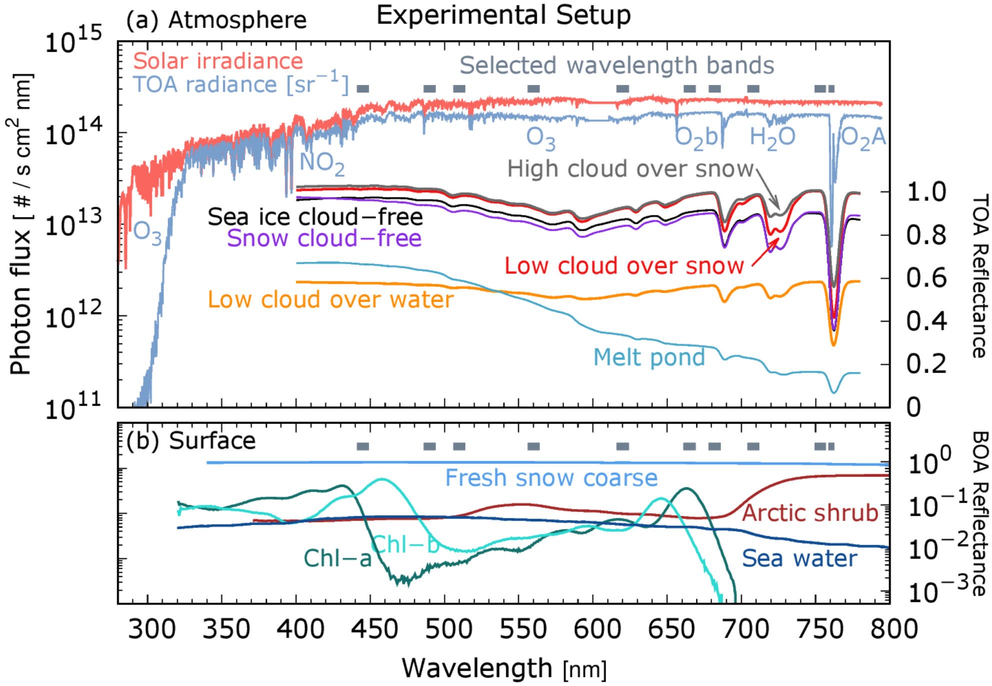

Figure 1. Plots of the solar irradiance, the radiance of a cloud (Earthshine) and reflectances at top (TOA) and bottom (BOA) of the atmosphere as a function of wavelength from 280 nm to 800 nm. The cloud radiance was observed by GOME on May 15, 2001 over Kara Sea (80.53°N, 75.99°E). Modelled R_λ^{TOA} (nadir, solar zenith 40°) display a water cloud, placed at 3 km and optically dense 30, above sea water and snow, with a cloud-free sea ice, snow and melt pond spectrum. The lower panel shows the black sky hemispherical reflectance at the ground of relevant Arctic surface components. Chlorophyll absorption is taken from Clementson and Wojtasiewicz (2019) and plotted for a May 2016 concentration of 12 mg m^{-3} observed in the Bering Sea (Frey et al., 2018). Arctic shrub and coarse snow data are taken from the ECOSTRESS and ASTER spectral libraries (Meerdink et al., 2019; Baldridge et al., 2009). Melt pond and sea ice albedos are from Istomina et al. (2013).

~~this situation, coupled with different sensor~~ , is not measured by these sensors. Because of the different sensors' swath widths, ~~limits the use of R_λ^{TOA} measurements up to a common north parallel for those months that guarantee adequate sampling. This effect is illustrated~~ the R_λ^{TOA} measurements in the solar spectral range have a northern latitude boundary (or terminator). This boundary is illustrated by plotting the pan-Arctic annual cycle of R_λ^{TOA} in Fig. 2. At the three wavelengths 510, 560, and 760 nm, the seasonality shows that summer months have lower R_λ^{TOA} and higher otherwise. ~~The~~ This darkening of the Arctic can also be seen by comparing the years at the beginning of the record, 1996, with the most recent ones. However, this ~~behavior occurs~~ behaviour occurs only between April and September. These are the months when the individual terminator of the three sensors reaches the latitude 85°N, this being the spatial threshold of common ~~coverage. For~~ spatial coverage we set in the monthly average. As shown in Fig. 2, the other months (October to March inclusive) ~~the individual terminators do not guarantee sufficient sampling (Fig. 2-c) and the R_λ^{TOA} curves~~ show that recent years are brighter (higher R_λ^{TOA}) than those at

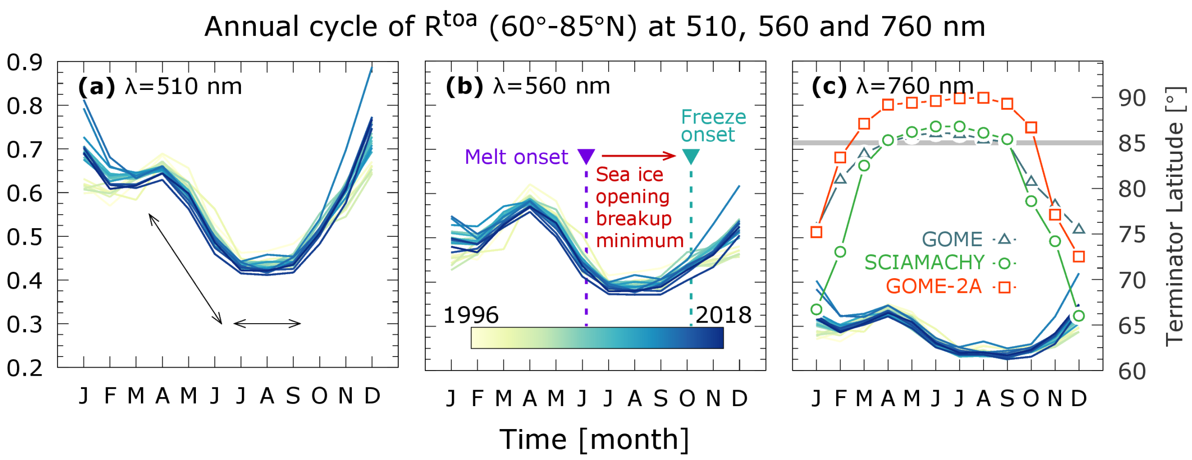

Figure 2. Annual cycle of spectral R^{TOA} at three wavelengths ($\lambda = 510$, 560, 760 nm) for the full record from 1996 to 2018. All sets exhibit the demarcation between months of steep (Apr-May-Jun) and flat gradient of R^{TOA} (Jul-Aug-Sep). This shift leads by one month melt onset (6 Jun), followed by sea ice opening, breakup, minimum (16 Jul – Sep inclusive), and freeze onset (4 Oct) as observed with satellite brightness temperatures (Smith et al., 2020). On the rightmost panel the terminator location of the three sensors with the 85°N (grey line) common threshold used for monthly R^{TOA} aggregation.

the beginning of the time series. This is because the individual terminators move further south (Fig. 2-c) and the coverage is considered insufficient for this to be studied further.

From Fig. 2 we identify two distinct behaviors of ~~R^{TOA}. One~~ R_λ^{TOA}. The first is a period of steepest decrease, from April to June, and ~~one relatively flat~~ the second is a plateau of relatively flat R_λ^{TOA}, between July and September. ~~In contrast to the common definition of the climatological seasons, we group April, May, June (AMJ) as Arctic spring and July, August, September (JAS) as Arctic summer. This distinction is explained by the sensors' measurement strategy and by the time-dependent physical processes leading to the transition between high-to-low Arctic reflectance in June to the minimum sea ice extent in September.~~ The changes in surface reflectance between April and May are attributed to snow cover changes and those in June to sea ice changes (Smith et al., 2020). Over water, the timing of such transitions increasingly approaches the summer solstice, which is the day of strongest solar insolation, while it moves further away from it over land (Letterly et al., 2018). It is therefore reasonable to regard this day as a ~~more natural~~ demarcation point between Arctic spring and summer.

In summary, we group April May June (AMJ) as Arctic spring and July August September (JAS) as Arctic summer. This distinction is explained by the sensors' measurement strategy and by the time-dependent physical processes leading to the transition between high-to-low Arctic reflectance in June to the minimum sea ice extent in September. We note that the definition of seasons is arbitrary and is determined by the breakpoints of the variable under consideration. In general, seasons can be astronomical, meteorological or climatological. Provided that our study deals with two decades of data, meteorological seasons are not useful and are not discussed hereinafter. The astronomical seasons for the Northern Hemisphere are AMJ for spring and JAS for summer (Cannon, 2005). Climatological seasons can be defined ad-hoc, one example being the Indian monsoon season stretching beyond the customary breakpoints (Fasullo and Webster, 2003). In our case, the fundamental motivation for defining ad-hoc Arctic seasons is then to ensure that the computed trends describe only those changes of R_λ^{TOA} caused by distinct underlying processes, which in turn determine the breakpoints in the time series of R_λ^{TOA} shown in Fig. 2.

2.2 Cloud and flux data products

In our study, the R_λ^{TOA} data is complemented by a record of cloud properties and broadband fluxes at TOA and BOA. These are inferred from the afternoon orbit (PM) of AVHRR sensors onboard the POES missions. ~~The primary~~ In spite of the availability of the morning orbit (AM) AVHRR series, we found that only the AVHRR PM series fulfilled the calibration stability requirements which allows trends' assessment to be made. Inspection of the time series of cloud properties and fluxes for the AM series showed that the drifts of the NOAA-12 platform before 2003, changing local overpass times, lead to calibration offsets and that the scan motor errors of the NOAA-15 platform to data gaps (Cloud_CCI Working Group, 2020).

One good reason for choosing ~~these records is the abundance~~ this AVHRR record is the number of studies using these data in the Arctic. ~~This has the required coherent radiometric calibration before the implementation of individual downstream methodology to assess changes across the Arctic.The cloud and flux records, version 3, are presented by Stengel et al. (2020) .~~ Our choice is driven by the maturity of the AVHRR data set of measurements, its popularity, and by its successful use by the advanced, most recent, retrieval algorithm exploiting it. This AVHRR data set is in its 3rd reprocessing and the algorithm used to generate it has 15 years of development starting with ATSR-2 onboard ERS-2. While improvements and validation have been documented in traceable documents (https://climate.esa.int/en/projects/cloud/key-documents/), the cloud and flux records are presented by Stengel et al. (2020, and references therein). Some features, that distinguish this data record from older AVHRR records, are as follows: i) the channels in the solar spectral range have been cross-calibrated with SCIAMACHY channels. SCIAMACHY is recognised for its accurate radiometric and spectral calibration. Because the part of our study dealing with R_λ^{TOA} is conceived in a way that the record is radiometrically coherent with SCIAMACHY (see App. A), this intra-band correction relates reflectance changes at visible wavelengths detected by SCIAMACHY to those by AVHRR, ingested in the cloud retrieval algorithm, which calculates τ and cloud albedo; ii) the cloud mask uses a neural network, trained on CALIOP data to take into account the extent of the underlying bright Arctic surface; iii) CTH has been calibrated using CALIOP profiles to account for the penetration depth of radiation inside a cloud. This is needed because the retrievals of CTH from all infrared thermal channels are influenced by this effect and yield a radiative cloud top height, lower than the physical cloud top.

The application of the cloud algorithm to MODIS measurements, ~~mimicking~~ which take place in the same wavelengths as the AVHRR channels, has shown that the retrieval scheme is well aligned with the reference standards of CloudSat and CALIPSO data for CFC, CTH, ~~COT~~ τ and liquid thermodynamic phase. While agreeing on the sorting of cloud tops between water and ice phases, higher ~~IWP variability~~ variability for IWP values lower than 50 $\mathrm{g\,m^{-2}}$ is found as compared to that in the reference DARDAR cloud data products (Delanoë and Hogan, 2010)~~. Aggregated IWP histograms do not~~ , but IWP histograms across the full range do not substantially differ (Stengel et al., 2015). Version 3 has improved version 2 in terms of precision, accuracy and stability (Stengel et al., 2017). Even more relevant to our purpose is the scheme adopted to calculate cloud properties and broadband fluxes. ~~CFC and optical property retrieval uses a neural network trained on CALIOP data to account for the extent of the underlying bright Arctic surface. CTH has been corrected with CALIOP profiles to~~

The broadband fluxes in the solar and IR spectral regions are computed solving the radiative transfer combining the two-stream approximation by Stephens et al. (2001) for the bulk bidirectional reflectance, transmission and source terms within a plane-parallel atmospheric slab and the spectral band model by Fu and Liou (1992) for gaseous absorption. Six bands in the SW and and 12 bands in the LW are calculated sequentially ingesting local properties of clouds retrieved with a Bayesian technique (Sus et al., 2018; McGarragh et al., 2018), which provides estimates of the individual uncertainty at pixel-level. Specifically, effective radius and cloud optical thickness are the primary inputs for flux calculations together with solar zenith angle and ancillary data from MODIS climatologies of visible and near-infrared surface albedo, linearly interpolated to each spectral band centre. Local vertical atmospheric profiles from ERA-interim account for the ~~depth of light penetration inside a cloud. The retrievals of CTH from all infrared thermal channels are influenced by this effect and yield a radiative cloud top height, lower than the physical cloud top. Broadband fluxes are not derived incorporating reanalysis data but the~~ p-T variations, while constant aerosol optical depth of 0.05 and concentrations of well-mixed gases are assumed, the latter being linearly interpolated for their time-dependent increase. The combination of the above factors yields an accuracy of $\pm 0.3\ \mathrm{W\,m^{-2}}$ in outgoing LW radiation (Christensen et al., 2016). The physical boundaries of clouds are additionally required to correctly compute scattering and absorption along the vertical. From the retrieved CTH and effective radius, the bottom cloud layer is calculated assuming a subadiabatic variation of cloud water path, separately for the liquid and ice phases. While this approach is appropriate for the shallow case (Merk et al., 2016), the thickness of deeper clouds is computed combining a variable increase of water content matching within-cloud temperature profiles. The nominal accuracy limit in this case is reached at temperatures less than 217 K ($-56\ ^\circ$C), which exceeds the yearly climatological range for the Arctic ($-25\ ^\circ$C February, $+2.5\ ^\circ$C July, Hersbach et al. (2020)), and AVHRR-derived cloub bottom height is found to be in good agreement within ± 369 m against ceilometer observations (Meerkötter and Zinner, 2007). Radiative transfer is solved twice. First all-sky fluxes are calculated with retrieved cloud properties ~~instead. This is important, because the changes in fluxes are coherently related to changes in the cloud properties.~~ and then the clear-sky fluxes, assuming that the pixel is devoid of clouds. This approach is in contrast to that employed with the MODIS cloud record and the CERES-EBAF radiation measurements at TOA, by virtue of which the interpolation of the measured clear-sky pixels serves as gap filling of all-sky pixels for the monthly aggregation of fluxes at BOA (Kato et al., 2013). AVHRR-derived fluxes at BOA have been validated by comparison with BSRN stations and the CERES-EBAF product (Stengel et al., 2020; Cloud_CCI Working Group, 2020). Given the standard notation (all = all-sky, clr = clear-sky, $^+$ = upwelling and $^-$ = downwelling fluxes~~F), the average~~), average comparisons with independent data show a good agreement for all downward fluxes and LW^+. The average long-term relative bias of AVHRR-derived fluxes against CERES ranges from +2.9% for ~~$F^{+,all}_{SW}$~~ SW^+_{all} to -2.7% for ~~$F^{+,clr}_{LW}$~~ LW^+_{clr}. Validation with BSRN measurements in the period 2003–2016 shows that the bias (correlation) for ~~$F^{+/-}_{SW}$~~ $\mathrm{SW}^{+/-}$ in range [-6.16,$+1.99$] ~~$\mathrm{W\,m^{-2}}$~~ $\mathrm{W\,m^{-2}}$ (0.93/0.99) and [-3.02,$+7.60$] ~~$\mathrm{W\,m^{-2}}$~~ $\mathrm{W\,m^{-2}}$ (0.99/0.99) for ~~$F^{+/-}_{LW}$ (Stengel et al., 2020).~~ $\mathrm{LW}^{+/-}$. In some locations, AVHRR-based estimates tend to be biased high for $\mathrm{SW}^+ < 100\ \mathrm{W\,m^{-2}}$ while the opposite holds for $\mathrm{SW}^+ > 250\ \mathrm{W\,m^{-2}}$ (Stengel et al., 2020) . This bias of higher spread can be due to the surface heterogeneity around the validation site, which influences the comparison of SW^{+} because of the difference in spatial scales between the satellite footprint and the BSRN effective point measurement. The surface treatment in the satellite record is also a potential source of error because SW^{+} is equal to SW^{-} times the surface albedo. While the actual sea ice extent is taken from measurements in the microwave (Henderson et al., 2013), a fixed value of surface albedo is assumed throughout the record. Consequently, intra-annual variability and long-term changes of surface reflectivity are not accounted for. This would lead to underestimate actual surface albedos in those months having fresh snow and ice (spring) and to overestimate during months of melting surface upper layers (summer). Cloud radiative forcing is dependent on fluxes at the surface. In the case of underestimation of surface albedo (or sea ice extent) we expect an overestimation of CRF and thus warming by the clouds and viceversa.

We do not expect differences in BOA fluxes as function of solar zenith angles because the instantaneous fluxes are corrected for the diurnal cycle of solar illumination by adjusting the surface albedo and the atmospheric path lengths. The LW fluxes have been also corrected by using a cosine function derived from measurements of the geostationary SEVIRI sensor. The final aggregation is a good approximation to a true 24h average (Stengel et al., 2020), needed to determine the true climatological mean of SW and LW fluxes and thus CRF. Consequently, also the seasonal averages (i.e. AMJ and JAS) are not expected to exhibit variations induced by solar zenith angle and directionality of surface reflection.

Misclassified cloudy scenes especially over dynamically bright surfaces (i.e. marginal and fractional sea ice zones) impact the calculation of broadband fluxes. This has been already noted in first studies comparing ERBE and AVHRR cloud radiative forcing derived with different scene classification schemes (Li and Leighton, 1991). The conversion of directional radiance, measured at TOA, to irradiance requires the knowledge of the angular light redistribution function of the surface and atmospheric components. If this conversion is not accurately ~~assumed~~performed, the irradiance and $\cancel{F_{SW}^{+/-,clr}}$ SW$^{+/-}_{\cancel{clr}}$ above reflecting surfaces cannot optimally be calculated. Using the same data of our study, it has been found a low sensitivity of trends in cloud radiative forcing to the biases in cloud properties over surfaces of changing brightness (App. d in Philipp et al., 2020, p. 7499). ~~This confirms the suitability of cloud properties retrieved from AVHRR measurements, classified with active sensor data, for Arctic trend studies.~~Specifically, Philipp et al. (2020) assessed possible uncertainties in CRF trends analysing CFC biases as function of sea ice concentrations (SIC) for the seasons of our paper. For season AMJ, the bias is systematically flat from SIC 0% to SIC 100%. Given that our trend model is based on anomalies and not absolute values (see App. B), any additive component of the bias cancels out and the resulting trend is not affected by it. For season JAS, the bias is not flat and a multiplicative bias in CFC can propagate to CRF via SIC changes. However, the SIC bins of Philipp et al. (2020, Fig. A1) can also be regarded as the SIC variance over one location in time, therefore this effect is relevant only for those locations with a large dynamic in SIC (e.g. the marginal sea ice zone). If the SIC anomalies over one location in the marginal sea ice zone are not equally distributed about zero, irrespective of any trend, but progressively change over time, their distribution is not Gaussian but skewed. This leads to add the time-dependent component in the CRF trend via CFC. Looking at Philipp et al. (2020, Fig. 8) the SIC anomalies for the marginal sea ice zone of the enlarged Chuckchi Sea are normally distributed. Upon regression, any possible residual of a non-normal SIC distribution, reflected in CFC and propagating into CRF, would still be captured by the trend model (see App. B) which accounts for the length of the effective independent sample in the record.

3 Results

3.1 TOA spectral reflectance

The R_λ^{TOA} time series, measured by GOME, SCIAMACHY and GOME-2A over the Arctic region (60–85°N), anomalies, trends and significance were harmonized (for more details see App. A and App. B). They are shown for wavelengths 510, 560 and 620 nm in Figs. 3 and 4. The R_λ^{TOA} retrieved from the sensors MERIS (on Envisat) and GOME-2B (on MetOp-B) confirm that the correction scheme is successful ~~.~~ for the spring (AMJ) and summer (JAS) months. The discrepancy between MERIS and SCIAMACHY in the fall and winter months, as long as sunlight is available, can be tracked to the different swath widths of the respective sensors. MERIS has a swath of 1150 km whereas SCIAMACHY has a swath of 1000 km. This implies that with the onset of the polar night at high latitudes, the western part of the scan of both sensors (which are polar orbiters in descending node) will include increasingly dark Arctic areas, the MERIS scan being more northward leaning. Therefore, any averages of MERIS measurements will include more dark scenes than those in an average calculated from SCIAMACHY measurements. For this reason, the MERIS reflectances in fall and winter months are generally lower than those by SCIAMACHY.

A consistent and consolidated data set results from the measurements of the three instruments. ~~Any errors are minimized, when sunlight availability across the Arctic provides full coverage for the sensors' swath at highest latitudes.~~ Seasonality is the dominant feature of Fig. 3. Maximum R_λ^{TOA} occurs in early AMJ when the Polar day results in the Arctic being fully illuminated and the ice extent is close to its maximum. Analogously, minimum R_λ^{TOA} occurs from August to September when the days are shortening and sea ice coverage is at its minimum. The observed seasonal cycle of R_λ^{TOA} agrees with that ~~observed~~ calculated by models as do the observations of sea ice extent over the Arctic (Holland et al., 2008). This provides evidence to confirm that one dominant parameter in R_λ^{TOA} variability is surface reflectance (Sledd and L'Ecuyer, 2019).

Figure 3 shows that the standard deviation of R_λ^{TOA} for GOME is smaller than the other sensors. GOME has a considerably coarser pixel size than the follow-on sensors (see Tab. A2). This leads to different mean R_λ^{TOA} and standard deviations because the integration time of the acquiring on-board electronics for a coarser pixel is longer than for a finer pixel. This averages out sub-pixel heterogeneity differently. We account for this effect by assessing R_λ^{TOA} trends not from mean values but from anomalies (see App. B) instead. The anomalies are customarily normalized with the standard deviation as a common technique for the analysis of records which might be heterogenous in scale, without changing the underlying sample distribution because standardization of anomalies is a linear transformation (Wilks, 2020).

~~A small~~ A negligibly small and statistically insignificant downward trend of R_λ^{TOA} for the three wavelengths in the solar range is seen in the anomalies of Fig. 4. The anomaly of R_λ^{TOA} is the difference between the value of R_λ^{TOA} and the climatological average value of R_λ^{TOA} at ~~time~~ the given time of the year t (see App. B). In a warming Arctic a statistically significant decrease in reflectance would have been expected due to sea ice loss. For water and ice-covered regions of the Arctic, Pistone et al. (2014)~~and Morrison et al. (2019)~~ , Morrison et al. (2019) and Morrison et al. (2018) state that no significant relationship between CFC patterns and ~~sea-ice~~ sea ice loss is observed during summer but some is identified in autumn months. Such changes are not observable in the pan-Arctic R^{TOA} anomalies. Rather, the reduction in reflectance is small and not attributable to a specific season. As a consequence, we need to ask whether the loss of reflectance associated with sea ice reduction is

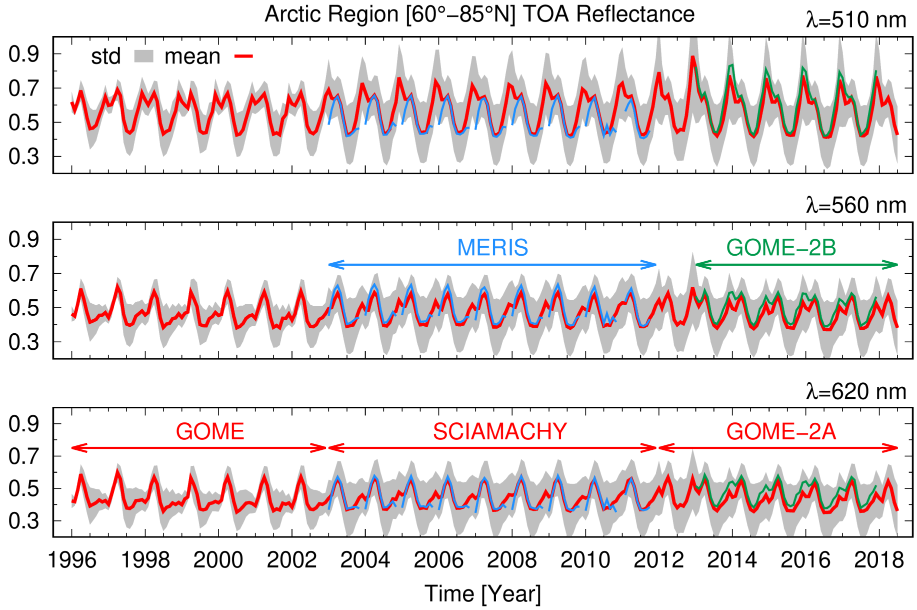

Figure 3. Time series of mean absolute R^{TOA} (red lines) and standard deviation (shaded grey) for the three wavelength bands 510, 560 and 620 nm derived from measurements of GOME, SCIAMACHY and GOME-2A ~~over the Arctic Circle~~between 60°- 85°N. The companion sensors MERIS on board Envisat (blue) and GOME-2B onboard MetOp-B (green) have been superimposed for comparison.

compensated by increasing CFC or brighter clouds~~and~~, at pan-Arctic and regional scale as well, and which processes lead to the small pan-Arctic R^{TOA} trends.

To answer these questions in the following, we map R_λ^{TOA} in the Arctic, gridded at $1° \times 1.5°$ latitude and longitude. Fig. 5 shows the spatially resolved R_λ^{TOA} trends for $\lambda = 510$, 560, 620 nm over the Arctic region for AMJ and JAS. The mean seasonal sea ice extent is superimposed and colored green for year 1996 and purple for 2017. Sea ice extent is identified as those surfaces with at least local 75% sea ice concentration. Data of sea ice concentration are from Walsh et al. (2019). Similarly, Fig. 6 shows trends for the analyzed wavelengths for the 12 Arctic regions, that are defined using the geographical subdivision proposed by Serreze and Barry (2014) and Wang and Key (2005a) (see Fig. B1). Trends for AMJ are shown in green and the JAS trends for selected spectral bands are shown in blue. The red symbols show the absolute averages of the R_λ^{TOA} values at the beginning of the record for the respective seasons.

There are marked regional differences. Those that are statistically significant (at 95% confidence level) are shown with red crosses. For AMJ a significant negative trend over the Barents Sea is compensated at all ~~four~~ three wavelength bands, by a positive R_λ^{TOA} trend over Greenland, the Canadian Archipelago and ~~Eastern~~ Western Arctic Seas. In JAS, the negative trend shifts towards areas of the Kara, Laptev and Chuchki Seas. These are Arctic areas having open ocean and are experiencing significant sea ice loss during the period of study. Statistically insignificant increases in R_λ^{TOA} are found over the boreal land masses. However, significant increases in R_λ^{TOA} are observed over Greenland and parts of the Arctic Atlantic sector.

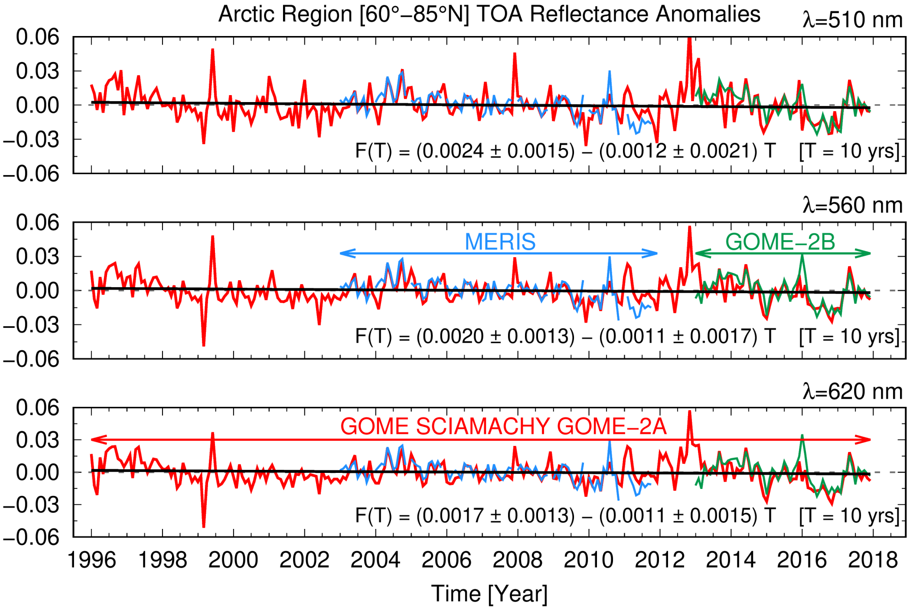

Figure 4. Time series of anomalies of R^{TOA} at $\lambda = 510$, 560 and 620 nm derived from the values of Fig. 3. The values are computed with a seasonal cycle on a sensor basis (see Eq. B1). The linear trend $F(T)$ is shown as black line with the bootstrapped intervals at 95% confidence.

~~Greenland exhibits positive trends of R_λ^{TOA} in the visible spectrum in both AMJ and JAS. This is not observed in any other region in the Arctic. The result~~ In general, the trends are negative and statistically significant in both seasons where sea ice retreats, such as in AMJ for the Barents Sea ~~is similarly extraordinary. Here the JAS trends of R_λ^{TOA} are strongly negative most likely due to~~ (Onarheim et al., 2018) and the perennial sea ice zone around the North Pole. For the remaining areas that cannot be directly explained by the difference in sea ice extent, we assume patchy residual sea ice concentrations below 50% closer to Eurasia and occurrence of melt ponds on the sea ice ~~loss (Onarheim et al., 2018), but the AMJ result is slightly positive. The values for the most eastern and most western Arctic Seas , i.e. East Siberian Sea, Laptev, Kara, Chuckchi and Beaufort Seas, are often clearly negative for the late summer (JAS) trends, while in AMJ the values show weaker negative or slightly positive trends~~pack. In both cases, open ocean areas and freshwater lower the albedo of the scene sensed by the satellites.

While areas with negative trends are spectrally neutral in both magnitude and statistical significance, areas of positive trends like the belt from the Canadian Archipelago, Beaufort and Chukchi Seas in AMJ and, to a smaller extent, Greenland in both seasons, show an increase in trend values and significance from 510 to 620 nm. While we cannot completely rule out the broadband influence of ozone trends (see App. D) on reflectances, the spectral patterns are coherent with an increase in some cloud properties conducive to snowfall and a brighter surface. Despite its proximity to the Canadian Archipelago, Baffin Bay has changes in R_λ^{TOA} trends that would more closely match the Eastern Arctic Seas region. Over the Hudson Bay, the R_λ^{TOA} trends show unusual patterns. They are largely positive in JAS and relatively strongly negative in AMJ. ~~During JAS the~~

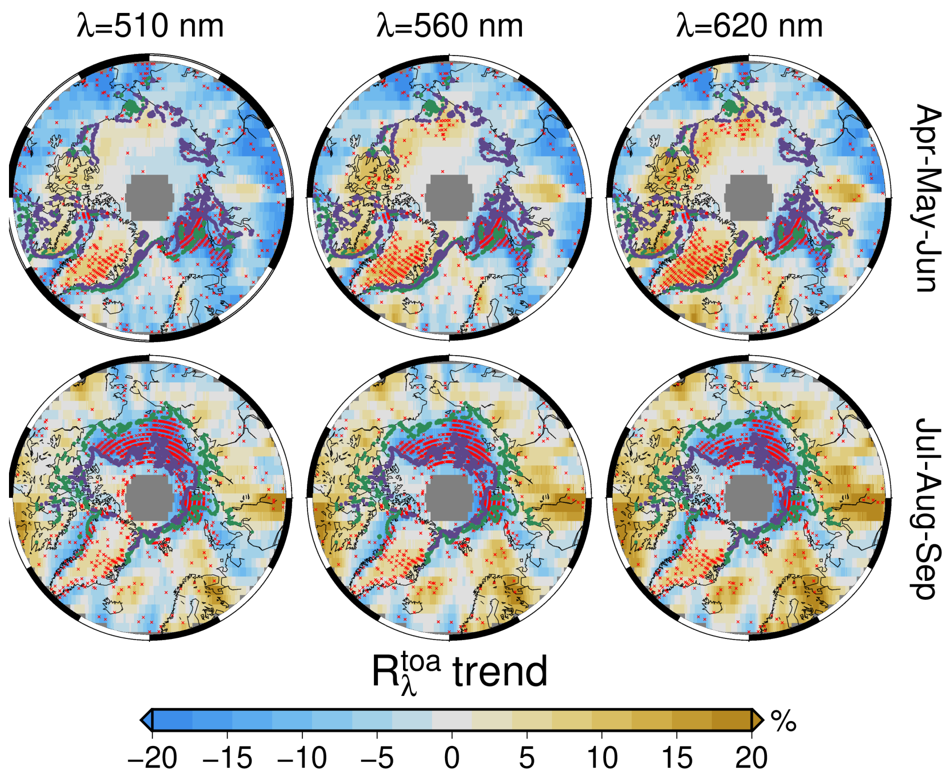

Figure 5. Seasonal $R^{\mathrm{TOA}}_{\lambda}$ trends for 1996–2018 at selected λ for Arctic spring (AMJ, top) and summer (JAS, bottom). The values are relative to the leading season of the record. Stippling in red indicates significant trends at 95% confidence. Sea ice extent (Walsh et al., 2019) for 1996 is outlined in green and for 2017 in purple.

~~trends for R^{TOA} = 760 nm are large. We infer that this results from a change in clouds, induced by either increased cloud height (CTH), cloud fractional cover (CFC) or albedo (CA).~~

Although not of the same magnitude, almost all regions show a reflectance change at ~~λ~~ 760 nm. This wavelength is the only channel with a very strong gaseous absorption and is not in the broadband continuum like all other channels. 760 nm bears more information on light scattering aloft than at the surface, because of the strong columnar absorption of atmospheric oxygen largely extinguishing photons before they impinge on the ground. Oxygen absorption is modulated primarily by CTH and, to a lesser extent, by CFC and optical properties such as CA and ~~COT~~ τ. In this context, where a positive trend value of $R^{\mathrm{TOA}}_{\lambda}$ at 760 nm is observed, greater than the other channels, we deduce a ~~particularly large number of statistically significant large trend values of $R^{\mathrm{TOA}}_{\lambda}$ are observedover Greenland during AMJ, which indicate a~~ clear change in occurrence of clouds or one of their physical or scattering properties. This is the case for Greenland during AMJ and JAS, for the Canadian Archipelago and the Barents, Chuckchi, East Siberian Seas only in AMJ, for the Barents Sea the Hudson Bay, the Atlantic corridor and the Siberian continent only in JAS. Knowing that R^{TOA} is influenced by scattering and absorption in the atmosphere (Sledd and L'Ecuyer,

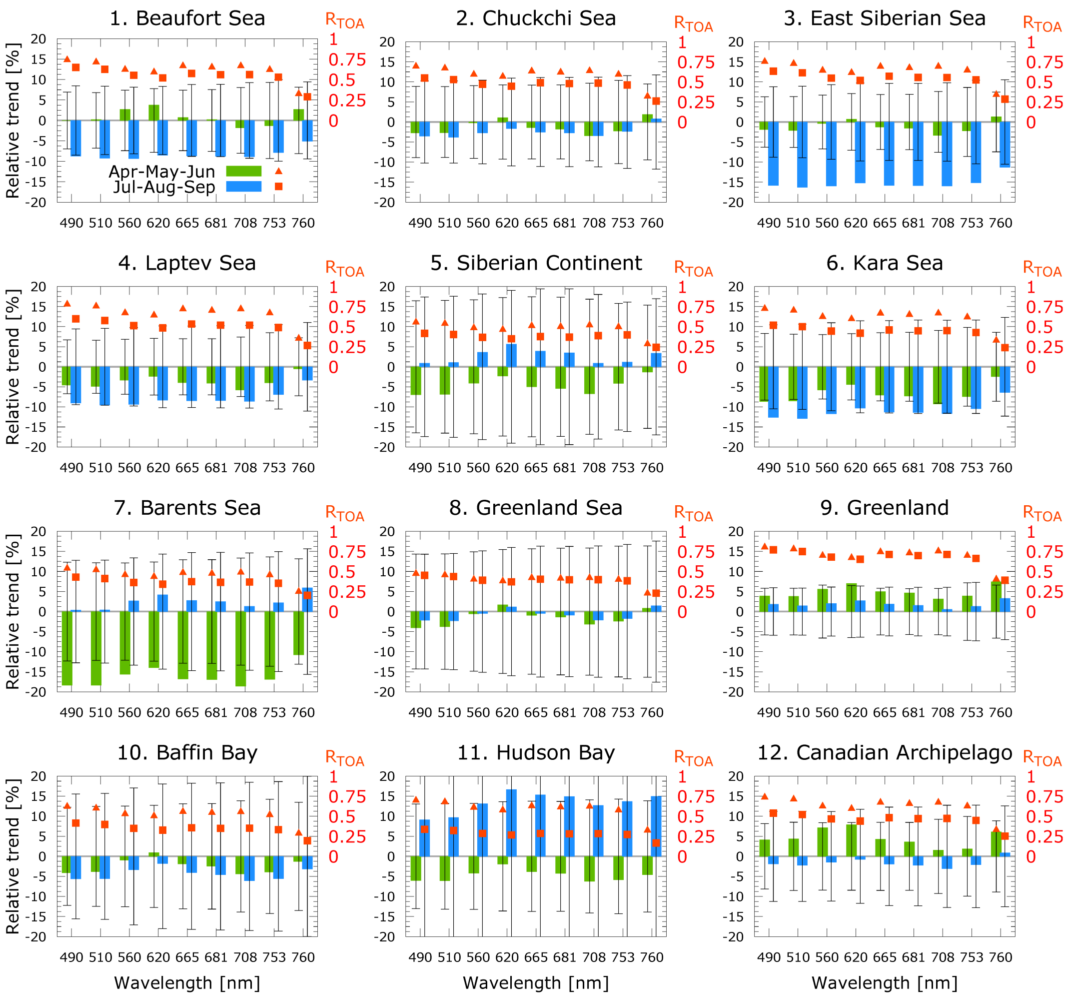

Figure 6. R_λ^{TOA} trends for the twelve regions defined in Fig. B1 for spring (AMJ, green bars) and summer (JAS, blue) months. The secondary y-axis display the absolute mean values of reflectance for each Arctic sector. The trend values are relative to the respective lead season and express the total change throughout the record.

2019; Donohoe and Battisti, 2011) and that the atmospheric R^{TOA} can be additionally partitioned into cloud, aerosol and gas contributions, this prompted us to examine changes in those cloud properties which directly influence the spectral R^{TOA} trends.

3.2 Cloud properties

The globally-validated and consolidated cloud record (Stengel et al., 2020) has first been analyzed across the Arctic (60°–85°N). The top ~~plot~~ panel of Fig. ~~8~~ 7 shows time series of CFC and CTH. Both parameters show small, statistically insignificant, trends over the last 20 years. CFC has slightly increased by about 0.001 (+0.14%) decade^{-1} while cloud tops are lower by ≈ 6 m (-0.14%) decade^{-1}. This finding obviously excludes an explanation being that reflectance loss at visible wavelengths, due

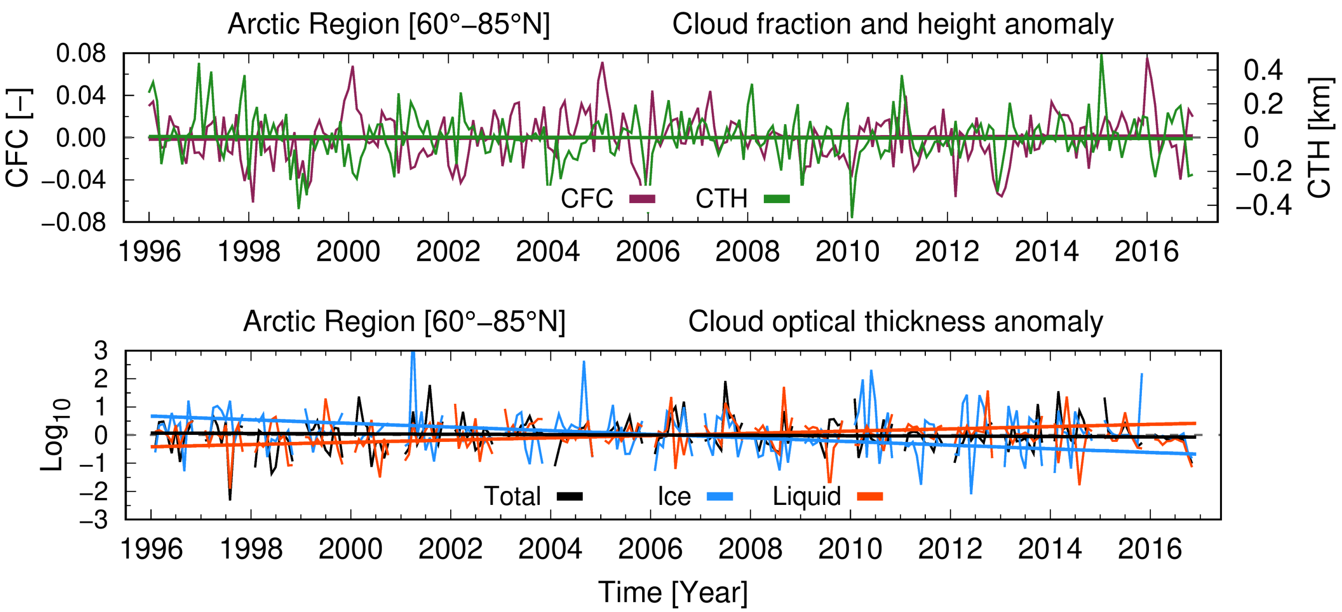

Figure 7. ~~For~~ Pan-Arctic anomalies and linear trends of cloud fractional cover (CFC), top height (CTH), optical thickness (COT, τ) of ~~warm~~ all, liquid, and ~~cold~~ ice clouds~~the left panel shows the pan-Arctic trends, while the right panel shows maps of their seasonal breakdown together with cloud albedo (CA) at λ=600 nm~~.~~The trend values in % are relative to the property value at the start year (1996) in the record. Stippling in yellow indicates statistical significance at 95% confidence.~~

Table 1. Pan-Arctic mean values in 1996, trend intercept, slope and bootstrapped 1-σ (given for 10 years time interval) for cloud fractional cover, top height and optical thickness τ of Fig. 7.

Cloud parameter	Mean 1996	Intercept	Slope
Fractional cover	0.695	-0.002 ± 0.003	$+0.001 \pm 0.007$
Top height [km]	4.395	$+0.006 \pm 0.022$	-0.006 ± 0.043
τ Total	12.554	$+0.070 \pm 0.889$	-0.067 ± 0.013
τ Liquid	14.056	-0.415 ± 0.177	$+0.398 \pm 0.348$
τ Ice	10.563	$+0.673 \pm 0.102$	$+0.645 \pm 0.201$

to shrinking sea ice extent, is offset by more CFC or that the loss of CFC reveals more bright underlying surfaces. However, the ~~middle~~ bottom plot of Fig. ~~8~~ 7 shows that over two decades the ~~COT~~ τ temporal trend of liquid clouds has the opposite sign of that of ~~cold~~ ice clouds. τ of liquid ~~warm~~ clouds increases, statistically significantly, by about 0.4 (+2.85 %) decade^{-1} while the ice-cloud τ decreases by 0.65 (-6.15 %) decade^{-1} in the same period. Altogether, total τ of clouds has not changed, meaning that clouds have experienced a net shift from the ice to the liquid phase without changing their total opacity. The mean values for 1996 and trends of the above cloud properties are given in Tab. 1.

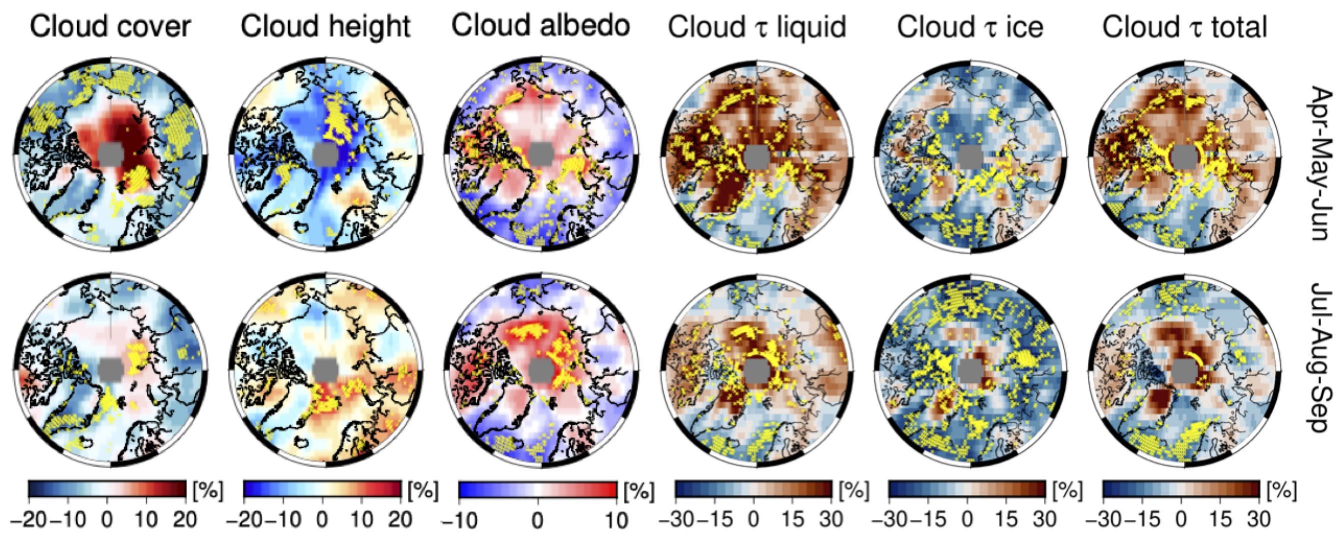

Figure 8. For cloud cover (CFC), height (CTH), cloud albedo (CA) at 600 nm, optical thickness (COT, τ) of all, liquid and ice clouds, the panels show their seasonal breakdown. The trend values in % are relative to the property value at the start year (1996) in the record. Stippling in yellow indicates statistical significance at 95% confidence.

Similar to the approach we used for the R_λ^{TOA} trends regionally and qualitatively, we map cloud parameters in the bottom panel of Fig. 8, adding also the albedo of clouds at $\lambda = 600$ nm. CFC trends are regionally partitioned and are seen to increase in the range 5–20% where the greatest sea ice losses are observed. This occurs during AMJ and less extensively in JAS. Examples of this behavior are found in the Barents, the Kara and Laptev Seas. On the contrary, large areas of statistically significant decrease in the range 2.5–10% are homogeneously observed across land masses circling the inner polar belt. This includes Greenland and the Atlantic corridor, confirming past results (Hofer et al., 2017). More pronounced trends of the different cloud parameters, irrespective of their sign, occur in AMJ rather than in JAS. The Hudson Bay is one of the few regions experiencing a seasonal trend reversal. The AMJ period is characterized by less cloudiness (-5%), whereas the JAS period exhibits an increase of the order of almost 10% over the last two decades. The resemblance to the trend reversal of all R^{TOA} channels (Fig. 6) indicates that CFC changes primarily modulate R_λ^{TOA} over the Hudson Bay. This is inferred from the absence of change of trend sign of those cloud parameters that influence the reflectance in the solar spectrum, such as ~~COT of~~ τ of liquid water and ice clouds ~~(third and fourth column~~ in Fig. 8).

CTH decreases, especially where statistically significant trends are observed, during AMJ across almost all sectors of permanent and marginal sea ice (Beaufort, Chuckchi, East Siberian, Laptev, Kara Seas) and over the Baffin Bay. In the last two decades CTH in these regions has decreased by 10% on average. In JAS, however, CTH increases significantly from the Fram strait, throughout the Barents and Laptev Seas, closer to the Pole, and western Siberia, with a ~~less pronounced positive~~ slightly negative trend for Greenland ~~(+4%) and a more pronounced one for the Hudson Bay (+8%), albeit non significant~~and the surrounding waters, the southern Baffin Bay (the Davis Strait), Beaufort and the East Siberian Seas. ~~Total COT~~

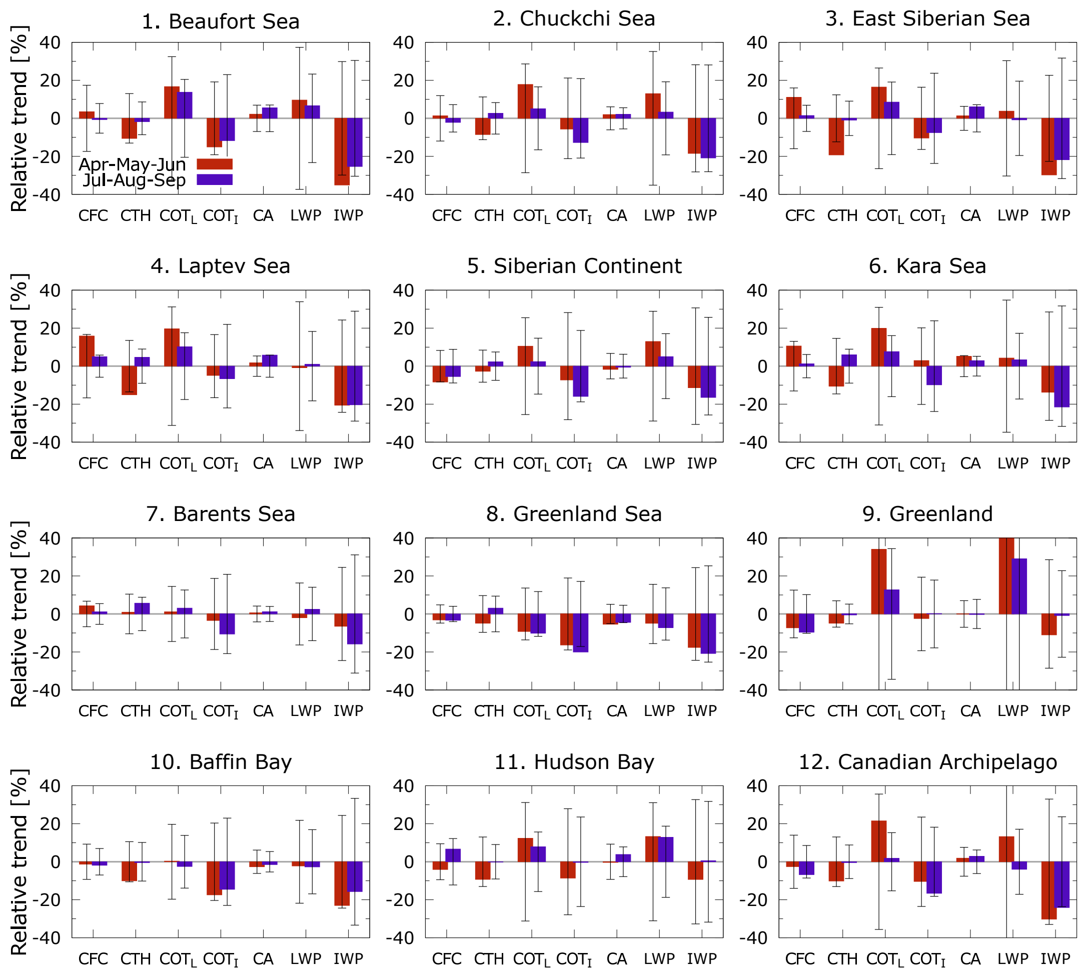

Figure 9. Trends (and 2-σ standard deviation) of cloud ~~properties~~ fractional cover (CFC), top height (CTH), optical thickness of liquid (COT_L) and ice phase (COT_I), albedo (CA), liquid and ice water path (LWP and IWP) for the twelve sectors defined in Fig. B1 for spring (April - May - June, red bars) and summer (July - August - September, purple) months. The y-axis display the change relative to the leading season in 1996 and express the total change throughout the full record~~throughout 2016.~~.

Total τ is split into liquid and solid cloud phases. The geographic distribution of the trends in Fig. 8 provides insight into which areas are responsible for the positive pan-Arctic trend in τ of liquid clouds (τ~~-water~~-liquid) and for the negative trend for ice clouds (τ-ice). τ~~-water~~ -liquid increases across the whole Arctic in AMJ except over the Atlantic sector and the southern part of the ~~Hudson~~ Baffin Bay. The positive trend is maintained over north Greenland, Canadian Archipelago, North Pole and part of the Eurasian continent also during JAS. A positive trend of τ~~-water~~ -liquid is correlated with a trend of opposite sign for τ-ice: this holds for all regions of permanent and marginal sea ice, for the Canadian Archipelago and for the Hudson Bay. ~~Conversely,~~ Greenland, Baffin Bay and the Atlantic sector show a different behavior: there is a 34% increase in τ~~-water~~ -liquid during AMJ and 22% increase in JAS. Notwithstanding the increase over ~~localized~~ certain areas (e.g. north Greenland), mean τ-ice over the Arctic regions remains nearly unchanged in ~~both~~ different seasons. The liquid phase of clouds does not increase across the Fram Strait, whereas the ice phase decreases by roughly 20% in both AMJ and JAS periods. Finally, the Atlantic sector (the Greenland and the Norwegian Seas) show decreases in the ~~COT~~ τ for both the liquid and solid cloud phase during AMJ and JAS.

The ~~rightmost~~ polar plots of ~~Fig. 8 show~~ seasonal trends in cloud albedo (CA) ~~, for which a marked change of the spatial rather than temporal scale is observed~~in Fig. 8 show that the magnitude of the positive trends in JAS is larger than those of AMJ but the spatial extent of the CA trend values are similar in both seasons. To a certain extent, the CA trends are geographically correlated with those of CFC and τ~~-water~~-liquid. Individual regions are grouped in a similar manner to the R^{TOA} polar plots: comparable distribution of CA are found over the most eastern and most western Arctic Seas (Beaufort and Chuckchi, East Siberian, Laptev, and Kara Seas). Positive trends are almost invariably distributed over water masses, the Canadian Archipelago and the northern part of Greenland, irrespective of the season. In contrast, clouds become ~~darker~~ less reflective at lower latitudes, southern Greenland and the Atlantic sector. Over the Siberian land masses this is not observed, and CA changes in the region ~~, besides being small,~~ are attributed to a competition between changes in CFC and τ~~-water~~-liquid. The loss of albedo due to cloud dissipation is compensated by the increment in albedo through increased τ~~-water~~-liquid.

To facilitate a quantitative seasonal comparison between the Arctic sectors, Fig. 9 shows the trends and the standard error (i.e. 2-σ standard deviation, see App. 2.2) of five cloud properties (CFC, CTH, τ of ~~water~~ liquid and ice phase, CA) together with the trend of liquid (LWP) and ice water path (IWP), from the same cloud record (Stengel et al., 2020). Changes in R_λ^{TOA} depend in the first place on changes in cloudiness and τ (irrespective of the phase), which in turn is a function of LWP, droplet/crystal effective radius ($\mathrm{r_{eff}}$) and air density ρ (i.e. $\tau = 3/2 \times \mathrm{LWP}/\rho\,\mathrm{r_{eff}}$). The sign of LWP and IWP trends confirm the τ trends. We infer that τ~~-water~~-liquid has increased as a result of the positive change of LWP and/or a concurrent systematic pan-Arctic decreasing trend of $\mathrm{r_{eff}}$ (see Fig. C1).

3.3 Cloud radiative forcing

We compute the net radiative forcing ~~, $\bar{F}^{cld}$ or CRF,~~ due only to clouds ~~. The flux data are taken from the cloud record (Stengel et al., 2020) (see App. 2.2). The difference between F^-~~ at the bottom-of-atmosphere, $\mathrm{CRF}^{\mathrm{boa}}$, from the differences between the downward and upward fluxes of SW and LW for all-sky and ~~F^+ is the net radiation $\bar{F}$ and CRF = $\bar{F}^{all} - \bar{F}^{clr}$.~~ clear-sky conditions as follows

$$\mathrm{CRF}^{\mathrm{boa}} = (\mathrm{SW}_{dn} - \mathrm{SW}_{up} + \mathrm{LW}_{dn} - \mathrm{LW}_{up})^{\mathrm{boa}}_{\text{all-sky}} - (\mathrm{SW}_{dn} - \mathrm{SW}_{up} + \mathrm{LW}_{dn} - \mathrm{LW}_{up})^{\mathrm{boa}}_{\text{clear-sky}}. \quad (2)$$

The multi-year mean and trends of SW~~, LW~~ $^{\mathrm{boa}}$, $\mathrm{LW}^{\mathrm{boa}}$ and total CRF~~at the surface~~ $^{\mathrm{boa}}$ are plotted in Fig. 10.

At pan-Arctic scale clouds exert a negative SW radiative forcing of -58.7 and -63.8 W m^{-2} in AMJ and JAS, respectively. In the same seasons, the LW component amounts to $+46.9$ and $+46.1$ W m^{-2}, and the multi-year mean of total CRF is -11.8

and $-17.6\ \mathrm{W\,m^{-2}}$. However, CRF is seasonally and regionally partitioned: clouds' total radiative forcing at the surface is positive over bright areas as a result of LW ~~offsetting SW~~effects offsetting SW effects. For instance, total CRF over Greenland is $+14.9$ and $+23.5\ \mathrm{W\,m^{-2}}$, which corresponds to the Arctic sectors over which ~~clouds reflect the least in absolute SW~~ the difference in SW CRF is the smallest (-19.8 in AMJ and $-21.3\ \mathrm{W\,m^{-2}}$ in JAS) ~~and emit~~ while LW CRF amounts to 36.2 in AMJ and 43.3 $\mathrm{W\,m^{-2}}$ ~~LW radiation~~ in JAS. The combined effect of the brighter surface and comparatively low optical τ (irrespective of the phase) over Greenland (8.4±7.3 in AMJ and 6.7±3.5 in JAS) increases SW reflectivity and damps upwelling LW. The minimum total CRF is measured over the Baffin Bay, the Atlantic corridor and Barents Sea in AMJ ($-51.1\ \mathrm{W\,m^{-2}}$) and JAS ($-43.4\ \mathrm{W\,m^{-2}}$). ~~This is explained by the combined effect of the brighter surface, increasing SW reflectivity and damping upwelling LW, and comparatively low optical COT (irrespective of the phase) over Greenland (8.4±7.3 in AMJ and 6.7±3.5 in JAS).~~ For the same seasons, darker surfaces of the Atlantic corridor and Baffin Bay imply the presence of open water masses, which have higher temperatures and, therefore, emit LW more effectively. However, SW offsets LW and total CRF turns negative owing to larger τ ~~water~~ -liquid over the Greenland Sea (14.5±3.4 in AMJ and 15.6±3.3 in JAS) or the Baffin Bay (14.6±5.3 in AMJ and 13.4±3.0 in JAS). At low surface albedos, typically less than 0.1 (Fig. 7 Shupe and Intrieri, 2004) , and for the majority of clouds SW CRF outweighs LW CRF, whereas SW radiative effects offset those by LW over higher surface albedos (>0.6), making CRF more sensitive to changes in cloud τ.

The climatological annual pan-Arctic total CRF (Fig. ~~D2~~D1) is positive at BOA ($+9.2\ \mathrm{W\,m^{-2}}$) with the sole exception of the Greenland Sea ($-4.2\ \mathrm{W\,m^{-2}}$). Minimum values are found over Baffin Bay ($+3.3\ \mathrm{W\,m^{-2}}$) and the Barents Sea ($+5.4\ \mathrm{W\,m^{-2}}$). Over the Arctic ocean, total CRF amounts to $+7.0\ \mathrm{W\,m^{-2}}$, which is lower than the $+10\ \mathrm{W\,m^{-2}}$ reported by Kay and L'Ecuyer (2013), while over land masses clouds warm the surface by $+11.0\ \mathrm{W\,m^{-2}}$. Consequently, the Arctic surface is warmed by clouds throughout and our results (Fig. D1) are qualitatively consistent with the current knowledge (Zygmuntowska et al., 2012; Kay and L'Ecuyer, 2013; Intrieri et al., 2002). The maximum cloud warming at BOA occurs over Greenland (AMJ $+14.9\ \mathrm{W\,m^{-2}}$, JAS $+23.5\ \mathrm{W\,m^{-2}}$) and to a lesser extent above sea ice covered regions in AMJ (East Siberian Sea $+6.9\ \mathrm{W\,m^{-2}}$, Beaufort Sea $+5.7\ \mathrm{W\,m^{-2}}$, Laptev Sea $+2.1\ \mathrm{W\,m^{-2}}$) and JAS (East Siberian Sea $+0.4\ \mathrm{W\,m^{-2}}$, Beaufort Sea $+6.5\ \mathrm{W\,m^{-2}}$). Otherwise, the other Arctic regions show a negative total CRF, from $-51.1\ \mathrm{W\,m^{-2}}$ over Greenland Sea and $-42.2\ \mathrm{W\,m^{-2}}$ Barents Sea in AMJ to the $-39.2\ \mathrm{W\,m^{-2}}$ over those regions influenced by the climate of low latitudes (Baffin Bay, Greenland and Barents Seas) and $-30.7\ \mathrm{W\,m^{-2}}$ and $-22.4\ \mathrm{W\,m^{-2}}$ over the Hudson Bay and Kara Sea in JAS, respectively.

From the CRF trends of the last two decades (Fig. 10), clouds over the perennial sea ice zone are increasingly cooling TOA (see Fig. D2) and BOA alike, while being neutral to positive over the Atlantic corridor and land masses at low latitudes. In AMJ months, maximal cooling trends at TOA (BOA) are for Kara and Laptev, up to -2.7 (-2.4) $\mathrm{W\,m^{-2}\,decade^{-1}}$, and extend along the Polar Circle up to the northern section of the Baffin Bay through the Chuckchi Sea, albeit dropping in magnitude to -0.9 (-0.8) $\mathrm{W\,m^{-2}\,decade^{-1}}$. During AMJ, clouds have increasingly cooled the Siberian land masses and the marginal sea ice zones at an average rate of $-0.4\ \mathrm{W\,m^{-2}\,decade^{-1}}$, with the Barents Sea undergoing the strongest CRF drop by $-2.5\ \mathrm{W\,m^{-2}\,decade^{-1}}$. Otherwise, the CRF trend at TOA and BOA during JAS varies from slightly positive over land masses, such as Eurasia, $+0.1$ ($+0.1$) $\mathrm{W\,m^{-2}\,decade^{-1}}$, over open waters in the Atlantic sector, the southernmost portion of Baffin Bay, and the Bering Strait. Cooling trends due to clouds are identified over Greenland for both seasons having a rate of $-0.5\ \mathrm{W\,m^{-2}}$

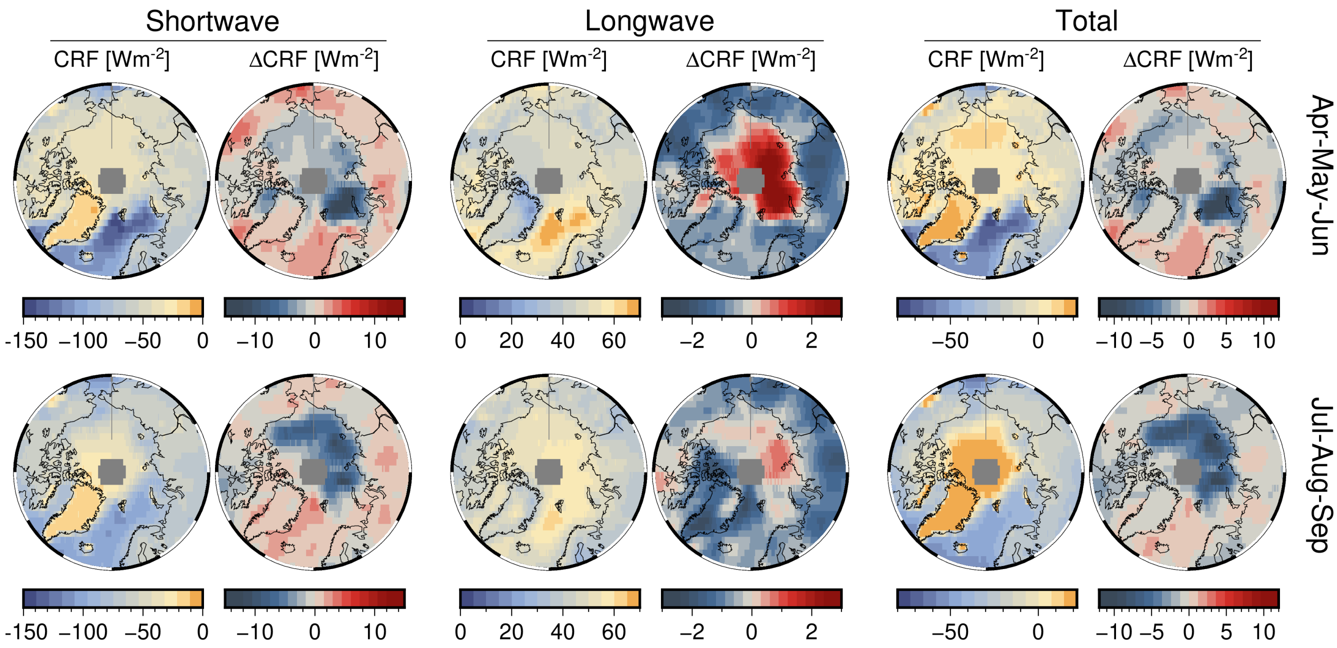

Figure 10. For Arctic spring (AMJ, top) and summer (JAS, bottom), the multiyear mean Cloud Radiative Forcing (CRF) and total change ΔCRF at the surface.

decade^{-1}. The influence of changes in surface albedo is manifested in these results. Where surface albedo remains almost constant (land masses, Greenland, and the Atlantic corridor) then CRF trends are of lesser magnitude. Instead, where the surface experiences more substantial changes, both seasonally and over the long term, trends in CRF are amplified, due to a greater influence of SW over LW.

4 Discussion

In the last two decades, the set of analyzed parameters provides a coherent geophysical picture: the Arctic $R_{\lambda}^{\mathrm{TOA}}$ has declined. However, this decline is less than that expected as a result of the loss of sea ice. We attribute the reason for this decreasing trend to be a decrease in sea ice, compensated for by ~~wetter~~ more liquid Arctic clouds. This results from their increasing liquid water content and a concurrent simultaneous decreasing ice content. Therefore, the thermodynamic phase separation of clouds is not only optical (Fig. 7) but also physical, considering Fig. 11. Indeed, the loss of IWP is larger than the increase in LWP. The cloud water path (CWP) is defined as the weighted sum of the two phases, whose relative occurrence is 0.54/0.46% in AMJ and 0.63/0.37% in JAS, for the liquid/ice clouds respectively. The seasonal correlation between CWP and its liquid/ice component is respectively 0.79/0.75 in AMJ and 0.57/0.84 in JAS, showing that the loss in ice water content is the main driver for the loss of total water condensate in clouds, more in summer than in spring. While highly variable at pan-Arctic scale, the total change in CWP amounts to -0.51 ± 11.01 % in AMJ and -3.66 ± 7.29 % in JAS. Notably, the majority of water path

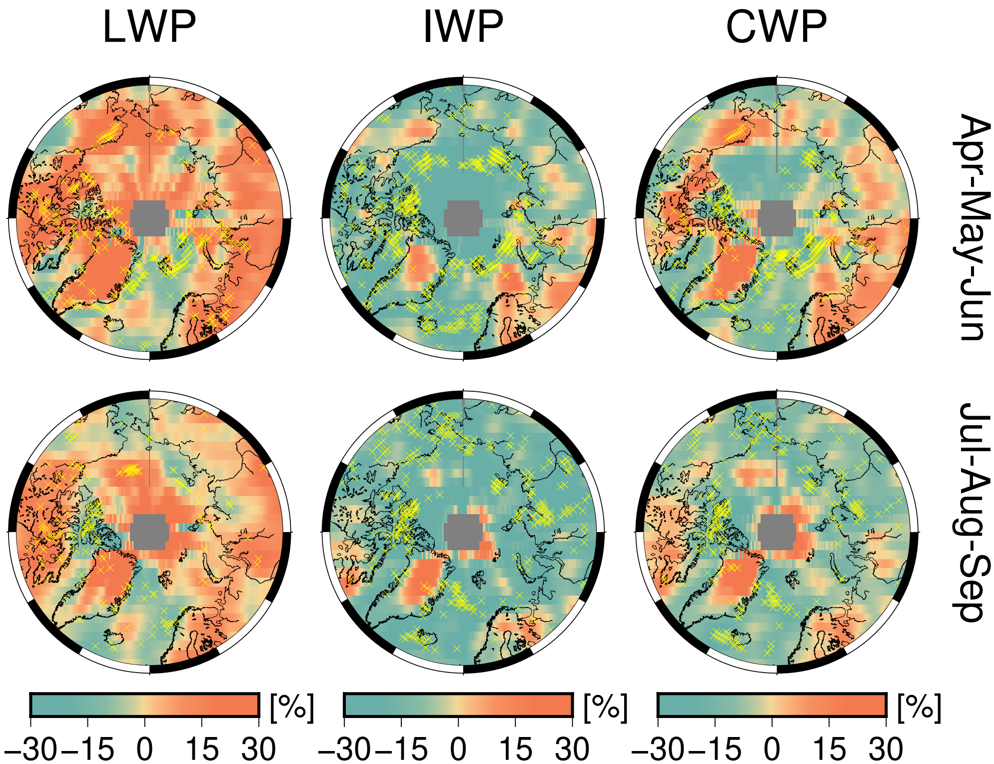

Figure 11. Seasonal total trend, from the first season in the record, of liquid, ice and total cloud water path (CWP). Stippling in yellow indicates areas of statistical significance at 95%.

changes exceeding natural variability are those of LWP/IWP decrease over areas of sea ice melting and only partly of LWP increase over land masses, Canadian Archipelago, some spots over Greenland and the Beaufort Sea in JAS. In light of the results presented so far regarding the optical thickness and separation of the two cloud phases, it is reasonable to assume that this trend will continue in the future, allowing more patterns of statistical significance to emerge even where they have not been detected with 20 years of data. Atmospheric moisture fluxes are increasing as a result of more open waters and transport (Boisvert and Stroeve, 2015; Rinke et al., 2019). Marked regionality and seasonality of R_λ^{TOA}, cloud properties and CRF across the Arctic is identified in four macro-regions, consistently ~~exhibting~~ exhibiting similar behavior: Greenland, the permanent and marginal sea ice areas, the Atlantic sector, and the land masses ~~al~~ at lower latitudes.

To some extent, Wang and Key (2005b) anticipate the results of our work. The downward trend in broadband albedo of -1.40% decade^{-1} between 1985 – 1999 is confirmed by our negative all-sky R_λ^{TOA} trends, implying a sustained sea ice loss after 2000 and general darkening of the Arctic surface. However, the regional patterns match neither our results nor most recent knowledge (Hofer et al., 2017). The annual increase of 0.6% in CFC over the Canadian Archipelago, Chuckchi Sea and Siberia and, in JAS, over Greenland reported in Wang and Key (2005b) is probably explained by the limited length of the analysed record. Trends in CFC over Greenland, for instance, level out before 1995 but turn strongly negative afterward, contributing to a significant loss of the ice shield mass (Hofer et al., 2017). This ~~explains~~ might explain the nonexistent clouds' τ trend in Wang and Key (2005b), which is in contrast to the significant moistening across most of the Arctic of Figs. 6, 8 and 9.

Greenland has a unique behavior: R_λ^{TOA} trends at all wavelengths are positive, irrespective of the season (Fig. 6). The AMJ R_λ^{TOA} trends, up to 5%, are even larger than those for JAS. This result is particularly surprising, given the insignificant CFC trend at pan-Arctic scale and the local negative CFC trend in both seasons (Fig. 8,9), thus not contributing to an increase of the overall reflectance. Therefore, we conclude that the increase in R_λ^{TOA} is due to the enhanced exposure of reflective surface in the southern part of Greenland, while a similar increase in the northern part is due to the simultaneous increase of τ-total (Fig. 8) and CWP (Fig. 11).

Similar behavior is found in the Hudson Bay and Canadian Archipelago, which show an increase in reflectance, in contrast to a general darkening of the Arctic. The mechanism by which these regions increase R_λ^{TOA} lies in the link between LWP and CA, through τ-~~water~~-liquid. In fact, τ-~~water~~-liquid changes sustain the correlated R_λ^{TOA} changes because of the non-linear relationship of CA to τ-~~water~~-liquid via LWP. It follows that a R_λ^{TOA} loss is overcompensated by ~~wetter~~ more liquid clouds in the northern sector and by increased snowfall in the southern part of the Greenland continent. Cloud LWP has increased by 28-30% over Greenland and by 14-16% over the Hudson Bay and the Canadian Archipelago, having positive τ-~~water~~-liquid trends of 30%, 14% and 22%, respectively. Notably, the seasonal behavior of τ-~~water~~-liquid, increasing over Greenland, is not associated with CFC loss and a positive CRF change in the last 20 years. In contrast, cloud dissipation, increased by anticyclonic activity and concurrent temperature inversion strengths, is responsible for enhanced insolation at the ground and melting (Hofer et al., 2017). In addition to cloud loss (Figs. 9,8 and Hofer et al. (2019)), extensive ice melt in Greenland is also known to be enhanced by low altitude liquid water clouds that have sufficient opacity to enhance downward LW flux, but are also optically thin enough to allow a significant amount of SW flux to pass through. This results in the surface being warmed (Bennartz et al., 2013). Such clouds occur in the LWP region between 10 $\mathrm{g\,m^{-2}}$ and 60 $\mathrm{g\,m^{-2}}$. Figure 9 shows that the increase in τ-liquid of clouds and LWP over Greenland in spring and summer is among the largest in the entire Arctic (ΔLWP $>$ 20-40%). In both seasons, the cloud fraction decreases and τ-liquid (as well as the LWP) increases spatially on average. Both effects impact upon the downward SW flux at BOA, but in the opposite direction, resulting in a small net positive change in SW CRF. For decreasing CFC over Greenland and in presence of an increase in near-surface temperatures, we expect a decreasing downward LW flux which might not be compensated by the LW enhancement by more liquid water in the clouds (Fig. 10, mid panel).

JAS R_{560}^{TOA} changes over the Hudson Bay are exceptional. They are correlated with a 9% increase in τ-~~water~~-liquid and minimal CRF changes. This area shows one of the largest CFC increases during JAS months (Fig. 9), also corroborated by similar significant changes in AMJ and JAS observed in the reanalysis data (Fazel-Rastgar, 2020). The total CRF is -30.7 $\mathrm{W\,m^{-2}}$ while $+2.7$ $\mathrm{W\,m^{-2}}$ during AMJ. CRF trends point to a cloud cooling of the Hudson Bay at a rate of -2.9 (AMJ) and -1.3 (JAS) $\mathrm{W\,m^{-2}}$ over the last two decades.

Cloud forcing at the surface depends on cloud property changes. The behavior is summarized in the seasonal and regional charts of Fig. 12, in which mean value and trend of SW, LW and total CRF are shown as function of τ-~~water~~-liquid of clouds, LWP and CFC changes. It is evident that the ~~strong relationships in AMJ and JAS~~ relationships between total CRF, ~~COT~~ τ, and LWP are more important in modulating radiation ~~than CFC. While~~ in JAS than in AMJ. This is the case when the underlying surface has still an albedo high enough to modulate CRF, as in spring months over regions with sea ice. With a decreasing surface albedo, as in summer months, SW CRF cooling dominates over LW CRF warming~~, CFC changes modulate mainly the LW portion of cloud radiation in both seasons.~~ . As a consequence, Arctic regionality emerges from the clustering of the regions, especially in AMJ and to a lesser extent in JAS. In the last two decades the net ~~energy radiating at the surface due to clouds~~ radiative effect of clouds on the surface is decreasing. Clouds cool the surface when ~~the upwelling SW energy dominates the downwelling LW radiation.~~ they diminish the net SW flux by more than they enhance the net LW flux. We note also that CFC changes modulate mainly the LW portion of cloud radiation in both seasons. In fact, the seasonal coefficients of determination r^2 of SW CRF by CFC trends is comparable to those by τ liquid trends. However, for the LW CRF, r^2 by CFC is higher than that by τ-liquid (CFC: AMJ 0.98 for both above ocean and all areas; JAS 0.87 above ocean 0.94 above all areas. τ-liquid: AMJ 0.39/0.02 above ocean/all areas; JAS 0.65/0.19 above ocean/all areas). This is the case when clouds become optically denser and hence more reflective.

Those regions characterised by a darkening surface undergo an increase in SW reflection, leading to an increasing cooling by clouds (ΔCRF<0). This takes place over the Barents Sea, a region characterized by early sea ice loss in AMJ and over the perennial sea ice zone (Beaufort, Laptev and East Siberian Seas), where a CRF decrease at a rate of $-$1-2 $\mathrm{W\,m^{-2}}$ is associated with greater cloudiness in AMJ and increasing τ~~-water~~ -liquid in JAS. Quantitatively, with values of $\Delta\mathrm{CRF_{Total}} = -1.4\ \mathrm{W\,m^{-2}}$ and ΔCF = 3.03 %, we obtain the total long-term sensitivity $\Delta\mathrm{CRF_{Total}}/\Delta\mathrm{CF} = -0.48\ \mathrm{W\,m^{-2}\ \%^{-1}}$ over the Beaufort Sea in AMJ. The sensitivities of the SW and LW parts of CRF amount to -0.56 and $+0.84\ \mathrm{W\,m^{-2}\ \%^{-1}}$. Although averaged over one multi-year season only, our estimation is in line with measurements reported at the same location during the SHEBA campaign (Shupe and Intrieri, 2004). The SHEBA sensitivity of $\partial\mathrm{CRF_{LW}}/\partial\mathrm{CF} = 0.65\ \mathrm{W\,m^{-2}\ \%^{-1}}$ was seen to offset the SW for most of the year (with $\partial\mathrm{CRF_{SW}}/\partial\mathrm{CF} \in [0,1]\ \mathrm{W\,m^{-2}\ \%^{-1}}$), thereby warming the surface while cloud cooling took place only in midsummer months. Accordingly, we report a net total (SW+LW) sensitivity of $-0.13\ \mathrm{W\,m^{-2}\ \%^{-1}}$ in JAS, meaning that the SW cooling takes over LW warming during the Arctic JAS in the record. The ~~greenhouse~~ warming effect from increased CFC in AMJ over these regions is ~~not~~ directly linked to the retreat of sea ice, the onset of which is in late May (Smith et al., 2020)~~. Rather it is attributed~~ , but also to the enhanced convergence of atmospheric water content originating from open Arctic oceans during years with anomalously low sea ice extent~~(Kapsch et al., 2013).~~ . Provided that the ocean can not be an appreciable source of water vapour in the Arctic boundary layer, Kapsch et al. (2013) attribute an increased downwelling LW flux to the increased atmospheric opacity as a result of convergence of moisture, in form of clouds and/or water vapour (Rinke et al., 2019). Our results imply that this mechanism is not only evident in the year-to-year variability of exceptional sea ice lows, but is also a long-term component at decadal time scales, during which atmosphere-ocean coupling effects are predominant.

With the sole exception of the East Siberian Sea in JAS where τ~~-water~~ -liquid of clouds grows in spite of a lower content of liquid water ($\Delta r_{\mathrm{eff}} \approx +0.3\%$, see Fig. C1), any positive τ~~-water~~ -liquid trend corresponds to LWP changes for both seasons ~~.~~ (see Fig. 12). Although not surprising, we note that the AMJ changes in CRF do not correlate with either LWP or ~~COT~~ τ. In

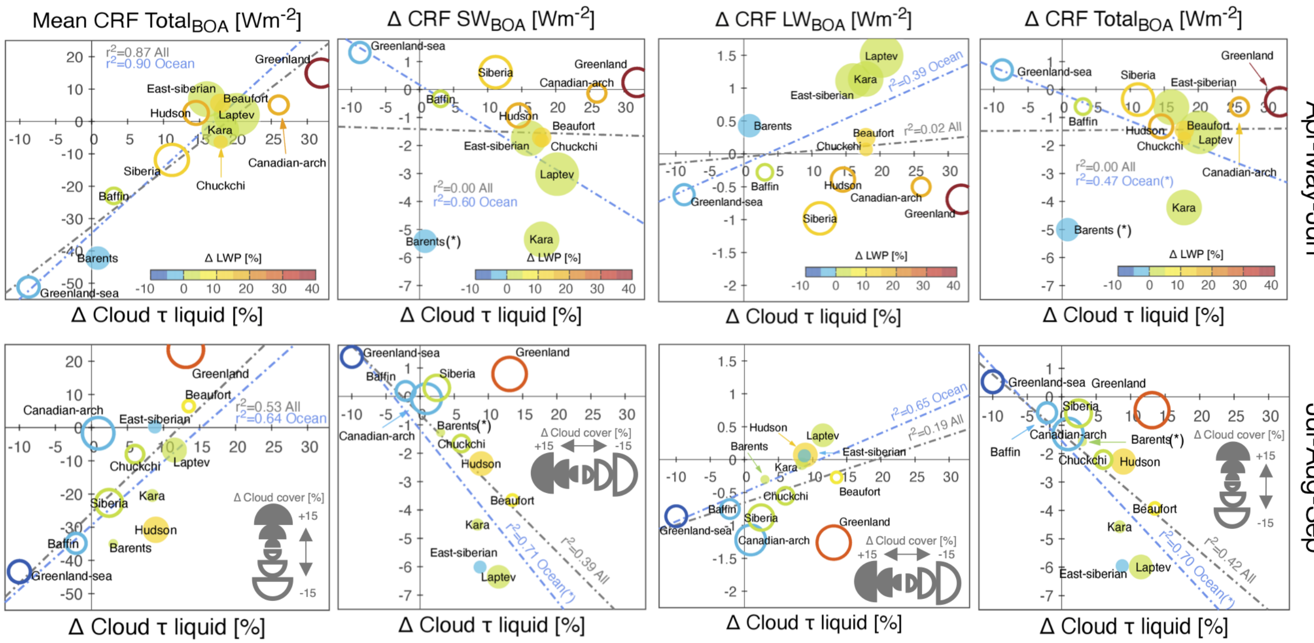

Figure 12. ~~Regional~~ From left ot right, regional and seasonal mean CRF~~(top left panel)~~, SW~~CRF (top right)~~, LW ~~CRF (bottom right)~~ and total CRF ~~(bottom left)~~ trends as function of τ trends for liquid clouds. The concurrent change in LWP is color coded while the increase (decrease) in cloudiness is given by a filled (outlined) circle.

the JAS months, however, larger cloud optical densities and LWPs are matched by a decrease in CRF at the surface. This is the ~~combined outcome of two effects: more insolation in the JAS months results in a more efficient SW scattering by cloud droplets and the~~ effect of darkening of the surface that lowers the LWP ~~threshold~~ value necessary for the CRF$_{SW}$ to dominate CRF$_{LW}$. Excluding Barents Sea, the ~~variance~~ variability of ΔCRF during AMJ is narrower (-4.2 to $+0.9\,\mathrm{W\,m^{-2}}$) than during JAS (-6 to $+0.4\,\mathrm{W\,m^{-2}}$). This is evidence for the importance of radiance from the underlying surface, which is larger in AMJ than in JAS.

~~In addition to loss of clouds, the extended ice melt in Greenland is also known to be reinforced by low altitude liquid water clouds having sufficient opacity to allow the enhancement of downwelling LW flux but also being optically thin enough to allow a significant fraction of the SW flux to pass. This results in the surface being warmed (Bennartz et al., 2013). Such clouds occur within the range of LWP between 10 g m^{-2} and 60 g m^{-2} corresponding to the range of enhanced CRF at BOA. Fig. 9 shows that the increase of cloud~~ Overall, the radiative effect of CFC and τ is expected to be similar, provided that their changes in time agree in sign. Because CFC and τ ~~-water and LWP over Greenland is among the largest throughout the whole Arctic for both seasons. We attribute a reduction in melting to the increased wetting of clouds (ΔLWP ⩾ 40% at current typical LWP values). Similarly, during AMJ, Greenland and the Canadian Archipelago exhibit a rather small ΔCRF along with a large increase~~ change in opposite directions, the decreases in LW CRF and increases in SW CRF suggest a dominant influence of

CFC rather than by water content in the clouds over Greenland. This CFC influence is still modulated, but not offset, by the changes in τ ~~-water and R_{560}^{TOA}. Enhanced surface cooling by clouds is thus less efficient. These regions are predominantly land or land/water mixtures, accordingly modulating the SW-to-LW flux balance.~~ and CWP.

Advances in observational techniques and process-level research are needed to assess unambiguously the relative roles of temperature T and atmospheric particulate matter in determining cloud thermodynamic changes. In the absence of a systematic, pan-Arctic, aerosol indirect effect due to decreasing trends of ice or cloud condensation nuclei (~~IN~~INP/CCN), higher condensation rates (i.e. positive LWP trends) of small-sized cloud droplets can only nucleate and grow by a combination of changes in Arctic boundary layer depth within a saturated air volume. Different temperature regimes influence CA changing the $\tau-\mathrm{r_{eff}}-$LWP relationship (Tselioudis et al., 1992) and favour droplet growth over condensation rates and vice versa (Lohmann et al., 2000). To this end, the driver of, mostly decreasing, $\mathrm{r_{eff}}$ trends (see bottom plot of Fig. C1) remains unclear. $\mathrm{r_{eff}}$ size spectrum is modulated by the amount of water vapor and available particulate. While model and satellite data show a general moistening of the Arctic (Rinke et al., 2019; Boisvert and Stroeve, 2015), local on-ground ~~(Graßl and Ritter, 2019) and pan-Arctic satellite (Linlu et al., 2021)~~ (Graßl and Ritter, 2019; Schmale et al., 2022) evidence of a decrease in total aerosol burden is growing. However, ~~IN~~INP/CCN can not be directly inferred from changes of column-integrated extinction of total aerosol load. Assuming a CCN decrease is in contradiction with the $\mathrm{r_{eff}}$ reduction via the Twomey effect. Alternatively, we speculate that the change in size spectrum or aerosol type might lead to optimal ~~IN~~INP/CCN size and hygroscopicity (Heslin-Rees et al., 2020), although the total aerosol amount has decreased. This could be the case when anthropogenic aerosols decrease because of emission policy, but natural aerosols increase due to more frequent boreal forest fires, increased sea spray and marine biogenetic activity as a result of more open waters (Schmale et al., 2021). Satellite-derived single $\mathrm{r_{eff}}$ values are only representative of the droplet/crystal population at a level of ≈ 1-τ from the cloud top (Platnick, 2000). We recommend that the available and relevant spectral observations are exploited (Kokhanovsky and Rozanov, 2012; King and Vaughan, 2012) to generate a pan-Arctic picture of in-cloud $\mathrm{r_{eff}}(\mathrm{z})$ profiles, which would optimally complement surveys based on spaceborne active techniques (Chan and Comiso, 2013; Matus and L'Ecuyer, 2017). $\mathrm{r_{eff}}(\mathrm{z})$ profiles, together with aerosol speciation at high latitudes (Schmale et al., 2021) and cloud bases (Lelli and Vountas, 2018), are essential in two ways. First, they constrain ~~IN~~INP/CCN activation, supersaturation and, therefore, cloud particle number concentrations (Zheng et al., 2015; Grosvenor et al., 2018). Second, cloud fields will be more accurately separated according to their phase (liquid, ice and mixed-phase) and layering (low, mid, high-level and multi-layered). We consider our results as upper bounds and more vertical resolution will improve our understanding of the evolution of clouds in the Arctic.

From a modelling standpoint, we can validate past results (Morrison et al., 2019), for which the increase in cloud τ ~~-water~~ -liquid and LWP are projected to extend well beyond the middle of the present century. Constraining the cloud microphysics and thermodynamic phase will not only be crucial to project future Greenland melting (Hofer et al., 2019) but also to assess the sign and strengths of total cloud feedbacks ~~(Gettelman and Sherwood, 2016)~~(Gettelman and Sherwood, 2016; Ceppi et al., 2016). Given the actual and future Arctic temperatures, ice will be increasingly depleted. Hence, τ ~~-water~~ -liquid and LWP will increasingly determine net cloud feedbacks (Bjordal et al., 2020). When the cloud ice phase turns to liquid water a negative feedback is expected due to the offsetting of LW by SW. This is especially true in those months characterized by low surface albedo, by virtue of a stronger interaction with atmospheric radiation by liquid cloud droplets than ice crystals. For the rest of the year when the surface albedo is high and Sun illumination is low or absent, the cloud feedack is expected to be more positive, that is a warming effect. If climate models do not correctly capture this behaviour, i.e they do not incorporate more supercooled liquid ~~than~~ and mixed-phase clouds (Lohmann, 2002), unrealistically large amounts of ice result, effectively ~~reversing the~~ contributing to the uncertainty in determining the sign of the net cloud feedback. We consider that this is one reason, which may explain in part the discrepancy between the atmospheric components (CAM) of the Community Earth System Model ~~2 (Gettelman et al., 2019, Fig. 2). We~~ (Gettelman et al., 2019, Fig. 2). While Huang et al. (2021) show that prescribing in the CESM1-CAM5 a weaker scavenging of supercooled liquid droplets by ice crystals in spring months leads to an increase in available atmospheric liquid water and a concurrent increase in downwelling LW flux at the surface, we note that a CAM5 positive cloud feedback at Arctic latitudes becomes negative in ~~CAM6~~ CESM2-CAM6 as a result of an improved modeling of the cloud phase. Coherently, CAM6 projects a warmer Arctic with increased rainfall rates in JAS at the ~~expenses~~ expense of snow precipitation (McCrystall et al., 2021), as the outcome of poleward moisture streams and ~~wetter~~ more liquid Arctic clouds.

~~In summary, we have identified expected decreasing and unexpected increasing trends of~~ Nevertheless, an improved representation of supercooled liquid clouds in CAM6 models (McIlhattan et al., 2020) does not necessarily result in better accuracy in describing cloud feedbacks. Although there is consensus that clouds, twice as bright in CAM6 than in CAM5, increasingly reduce the amount of SW energy accumulated at the surface through optical thickness and phase feedbacks (Goosse et al., 2018), thereby slowing the Arctic sea ice albedo feedback by 5 years over oceans and 2 years over land (Sledd and L'Ecuyer, 2021a), there are indications that clouds might accelerate the albedo feedback in some CAM6 models (Sledd and L'Ecuyer, 2021b). This holds in summer months when the atmospheric contribution to Arctic TOA albedo, dominated by cloud reflectance, is higher than that of the surface. While suboptimal prescribed covariability of clouds with the underlying sea ice is not ruled out, Sledd and L'Ecuyer (2021b) indicate that future efforts should focus on understanding the parameterization of the cloud microphysics, especially for those models that show a decrease in atmospheric reflectance.

5 Summary and conclusions

In this paper we focused initially on creating a record of spectral reflectance at the top-of-atmosphere - R_λ^{TOA} ~~during the period~~ - in the solar spectral regions to investigate changes in Arctic albedo in the last two decades. The spaceborne hyperspectral sensors employed in this work are now well equipped for this task, because their record of radiances has been continuously calibrated and reprocessed, reaching the needed maturity to serve as observational foundation for trend studies. Another advantage of this record of reflectances is that they are direct measurements, realization of basic physical processes, and are not dependent on algorithmic assumptions. Contrary to common knowledge, we grouped April May and June (AMJ) as Arctic spring and July August and September (JAS) as Arctic summer. This choice was justified by looking at the annual cycle of reflectances, which indicates that R_λ^{TOA} is largely determined by two distinct processes in AMJ and JAS, namely sea ice melting in AMJ, causing a high-to-low R_λ^{TOA} signal, and by changing cloudiness in JAS, flattening the reflectances until September. The calculated trends shall reflect this distinction.

In spite of the melting of ice, we find in spring and in summer decreasing pan-Arctic trends of reflectance, which are smaller than that we expect for the reduction of the surface albedo averaged over the Arctic. Then, we opted for a detailed regional-scale analysis, because numbers at pan-Arctic scale conflate trends of different magnitude and sign and are little informative, owing to the range of geophysical features characterizing the Arctic environment. In fact, the breakdown of R_λ^{TOA} trends reveals regional clusters of behavior. The periennal and marginal sea ice zones (from the Beaufort Sea until the Laptev Sea) have increasingly reflected less light in both seasons, being the JAS trends generally those of greater R_λ^{TOA} decrease. The Barents Sea exhibits statistically significant losses already in AMJ and a moderate increase of reflectance in JAS, both indication of sea ice loss and subsequent change in cloud properties. Greenland showed a statistically significant increase in R_λ^{TOA}, irrespective of the season, which could not only be explained by a greater exposure of glaciated ground upon loss in cloud cover.

We complemented the study of R_λ^{TOA} with that of available cloud data products from passive satellite remote sensing in the Arctic bewtween 1996 ~~to 2018 in the Arctic. We then investigated the possible origins of the unexpected increases of~~ ~~R_λ^{TOA}, analyzing cloud optical~~ and ~~physical parameters. We conclude that clouds, through changes in their optical properties~~2016. While cloud cover, height and total optical thickness have not appreciably changed over the last two decades at pan-Arctic scale, we found a statistically significant increase of the liquid phase of clouds, balanced by a similar decrease of the cloud ice phase. Therefore, the R_λ^{TOA} increase can be partly attributed to an increase in cloud reflectance, consequence of the more reflective population of cloud liquid droplets than ice crystals, this especially holding in summer months when the atmosphere is radiatively decoupled from a relatively dark surface. Similarly, the total mass of condensed water in clouds has not changed, but a net shift to the liquid phase took place at the expense of the ice phase. Regionally, the net change to more liquid clouds affected almost equally Greenland, the marginal and periennal sea ice zones in both seasons, and the land masses at lower latitudes but only in AMJ. In contrast, the North Atlantic and the southern areas of the Barents Sea have seen a decrease in both optical thicnkess and water path of both phases.

The resulting changes of total cloud radiative forcing at the surface indicate that over regions of melting marginal sea ice of transitional (high) albedo, the net effect is to increasingly cool the surface. This is the result of SW (cooling) effects offsetting LW (warming) effects in both seasons, being this less pronounced in AMJ than in JAS. Locally, clouds have increasingly warmed the surface over the periennal sea ice pack, the North Atlantic and the land masses at lower latitudes in both season, albeit at different rates, due to the relatively stable albedo of the surface. We have found a distinct relationship between trends in cloud radiative forcing and cloud properties. Cooling trends are attributed to the increase in optical thickness, mostly driven by positive trends in liquid water path, over increasingly less reflective areas. At the same time, cloud cover changes seem to regulate mostly LW effects than SW effects.

Concluding, while the climatological effect of Arctic clouds over sea ice is to warm the near-surface air positively contributing to Arctic Amplification, clouds also largely explain the increase in R_λ^{TOA} through changes in their optical properties and that implies an increasing amount of supercooled liquid cloud droplets. The higher reflectance of clouds results in a more negative radiative forcing at the surface, thereby locally dampening Arctic Amplification~~.~~, especially where sea ice retreats. In this paper we see a corresponding first signature of this tendency, that will become even more obvious in the future, because the sea ice is expected to decrease even further in the years to come. However, cooling by clouds implies the strengthening of the meridional temperature gradient. ~~We expect this~~ This will lead to increase the inflow of warmer and moister air masses from the lower latitudes into the Arctic climate. This may then either further decrease Arctic Amplification by generating more supercooled liquid water cloud, or possibly enhance Arctic Amplification by the ~~increase~~ increased input of warmer air, or some combination of the two. Future model projections of the Arctic climate must take into account these effects to accurately predict the impact of anthropogenic emissions of greenhouse gases and short-lived climate pollutants.

Appendix A: Detailed description of reflectance data harmonization

Table A2 shows that overpass time, swath and footprint size differ among the sensors used in this work. These sensors are payloads on satellites which fly in sun synchronous orbits having different equator crossing times. Errors in the R_λ^{TOA} in the Arctic arising from the 30-minutes time lag are considered negligible for averaged R_λ^{TOA}. Monthly aggregation leads to higher means for finer spatially-resolved instruments than otherwise. Thus, intra-sensor radiometric R_λ^{TOA} harmonization is a prerequisite for the creation of calibrated time series and the detection of trends. Different application-dependent approaches have been already employed. Krijger et al. (2007) derives gain correction factors based on the number of cloud-free scenes as a function of spatial resolution for maximization of usable trace-gas retrievals. Tilstra et al. (2012) separates the influence of scattering geometry and cloud occurrence to correct SCIAMACHY reflectances for the computation of the aerosol absorbing index at UV wavelengths. Both approaches are not suited for our goal. The former aims at the removal of the influence of clouds, which are a primary component of the Arctic environment. The latter examines instrumental performance in a spectral region that is not of direct interest as a result of potential radiometric degradation of sensors and of higher sensitivity to aerosols, whose radiative effects are comparatively small in the troposphere. Conversely, Hilboll et al. (2013) elaborate a method to explicitly take into account the difference in the ground pixel size and spatial misalignment across sensors. This is achieved by projecting the orbit of one instrument onto that of a second instrument. In our case, we select SCIAMACHY as reference sensor due to its well-calibrated spectral behaviour and because it overlaps with both GOME and GOME-2A. A conservative area-weighted remapping scheme Jones (1999) is employed to derive the factor matrix transforming GOME-2A reflectances as they were measured by SCIAMACHY. Due to the frequent overlaps at high latitudes, only those GOME-2A orbits closest in time to SCIAMACHY are remapped. To extend the time series beyond the loss of Envisat in April 8th, 2012, full SCIAMACHY geolocations, comprising 431 orbits per month, have been used as target tessellation for the rest of the GOME-2A record. The downside of mimicking SCIAMACHY orbits, due to its design of alternating nadir and limb swath states, is the reduction of the GOME-2A sampling rate. This is compensated for in part by the inherently different cross-swath viewing geometries and changes in illumination. GOME projection onto SCIAMACHY has not been implemented. Not only do the two sensors overlap for a limited period of six months, but the relatively low sampling rate of GOME would have resulted in suboptimal statistics, even at a monthly scale. Validation has shown that GOME R_λ^{TOA} are consistent with those of SCIAMACHY (see Fig. 3 in main text). Remaining intra-sensor inconsistencies that cannot be compensated for, such as changes due to the dynamic radiometric response over dark-to-bright surfaces, will be eventually accounted for by the trend model.

We tested the assumption that bidirectional surface effects do not introduce error in the detection of the temporal trends of R_λ^{TOA} by inspecting monthly distributions of the scattering angle throughout the record, separately for each sensor. This is needed because R_λ^{TOA} is, by definition, a directional quantity and depends on the scattering geometry~~. It has been found that the monthly data aggregation of all individual line-of-sights almost fully cover the hemispheric solid angle, incorporating the hot spots of different scene types . The~~ , that is on the phase function of different surface types and on the thermodynamic cloud phase. Across the Arctic, the mean value of the scattering angle of 98.48° in 1996 shifts to 98.41° in 2018 for AMJ (-0.08%) and from 97.03° to 96.55° for JAS (-0.51%). These shifts are due to a change in configuration of GOME-2A on July 15 2013, allowing tandem operation with GOME-2B. The GOME-2A swath width of 1920 km has been reduced to 960 km, halving the across-track pixel size and, consequently, sampling differently the viewing zenith (Munro et al., 2016). However, these shifts are considered uncritical for this study and do not introduce artefacts in the record.

Appendix B: Trend and significance estimation

Trend detection is performed with the same technique for all the variables and parameters in this study. We illustrate the steps with reflectances. Dropping the subscript λ for readability, the R_λ^{TOA}, measured by sensor i and aggregated at month t, $Y(t,i)$, are modelled with

$$Y(t,i) = \mu_i C(t,i) + S(t,i) + \omega_i t + \delta U(t,i) + N(t,i). \tag{B1}$$

The $\mu_i C(t,i)$ are the intercept of the regression line, $S(t,i)$ is the seasonal component of the time series, ω_i the desired trend value and $N(t,i)$ the noise residuals embedded in the model after the regression is carried out. The term $\delta U(t,i)$ stands for the product of the level shift δ among the respective sensor records (Hilboll et al., 2013) with the step function $U(t,i)$ needed to concatenate the individual time series at time $T_i(t=0)$ (Lelli et al., 2014). The seasonality $S(t,i)$ is accounted for by subtracting the average R_λ^{TOA} of each month from the respective monthly value. This method is similar to the harmonic expansion in Fourier series, in which the coefficients are derived in a least squares sense. Both methods are equivalent and the choice of one method rather than the other does not introduce significant errors (Mieruch, 2009). The term $\delta U(t,i)$ is embedded by calculating the seasonality separately for each instrument. Its function is to correct possible artefacts due to the different overpass times of the respective spaceborne platforms. While the offsets $\mu_i C(t)$, centred about their mean absolute value at the beginning of the time series, tend to zero upon the anomaly calculation, the last unexplored portion of the data is the noise component $N(t,i)$, in which autocorrelative effects are buried. The R_λ^{TOA} time series are persistent in time and the autocorrelation $\rho \nrightarrow 0$ for all Arctic regions after one lag. Thus, not all noise components of the record are random and cannot be treated as gaussian. This limits the informative value of any significance test and hinder the detection of trends. Block bootstrap resampling (Efron and Tibshirani, 1993), belonging to the group of nonparametric methods, does not require prior knowledge of the analytical form of the underlying statistics of potentially non-normal data (Mudelsee, 2010). They rest on the block length of the effective independent random sample (Wilks, 1997, Eq. 19). An empirical sample distribution of the trend magnitude ω is then computed scrambling n times the blocks of the original record. The resulting empirical distribution approximates the unknown ω probability density function. This allows to find the 2-σ_ω interval needed for a confidence level at 95%. For all locations where the ratio $|\omega/\sigma_\omega| > 2$, the trend magnitude ω exceeds natural variability and is termed statistically significant.

Appendix C: Uncertainty propagation in the cloud record and sensitivity

The cloud data set is generated using an optimal estimation framework, which allows propagation of random and systematic uncertainties into the pixel-based retrievals. Following Eqs. 2–5 in Stengel et al. (2017), for each location i at time t, we calculate the true variability $\sigma_{\mathrm{true}}(i,t)$ and the uncertainty of the mean $\sigma_{\langle x\rangle}(i,t)$ for the cloud property x from the mean of the squared pixel-based uncertainties $\langle\sigma^2(i,t)\rangle$ and its standard deviation $\sigma_{\mathrm{SD}}(i,t)$. Further, aggregation into monthly averages requires the uncertainty correlation c, or heterogeneity, relating $\sigma_{\mathrm{SD}}(i,t)$ to $\sigma_{\mathrm{true}}(i,t)$. Because c is not known beforehand, setting it to a fixed value is an arbitrary choice that does not account for the spatial and temporal relationship of algorithmic errors at pixel level throughout wide-scale cloud fields. Hence, we exploit the fact that $\sigma_{\mathrm{SD}} \to \sigma_{\mathrm{true}}$ when $c \to 1$. This holds when the spatial sampling is the highest, thus we scale the number of successful retrievals of the cloud property x to $c \in$ (0,1] and compute the c-dependent $\sigma_{\mathrm{true}}(i,t)$ and $\sigma_{\langle x\rangle}(i,t)$. Temporally, both σ_{true} and $\sigma_{\langle x\rangle}$ change as function of c. Seasonal trends of c reveal an overall increase of maximum 3% in AMJ and 1.9% in JAS over the Barents throughout the East Siberian Sea, whereas c over Greenland, Hudson Bay and the Canadian Archipelago exhibits a decrease of 0.6% in both seasons. This translates into a change of $\pm$0.5% and $\pm$0.4% in σ_{true} and $\sigma_{\langle x\rangle}$, respectively. With this approach, the clouds' heterogeneity of the monthly averages is related to retrieval errors predominantly in the spatial but not in the temporal dimension. Limited to an observational analysis of the cloud record, while uncritical for trend assessments only, $\sigma_{\langle x\rangle}$ can be then successively used to label as meaningful those sensitivities of CRF to susceptible cloud property x, whose trend exceeds $\sigma_{\langle x\rangle}$.

Appendix D: Additional description of ozone trends

R^{TOA} trends at 560 and 620 nm capture the Chappuis ozone absorption band having a broadband maximum centred about 602 nm and two wings stretching between 525 and 675 nm (Gorshelev et al., 2014). Analysing seasonal stratospheric and total column ozone, we are able to determine an effective modulation of R^{TOA} trends by ozone. Ozone data in Fig. A1 are locally derived from GOME, SCIAMACHY and GOME-2A (Coldewey-Egbers et al., 2005) for the total column values (Coldewey-Egbers et al., 2005) and with SCIAMACHY and the OMPS Limb Profiler measurements for the stratospheric column portion (Flittner et al., 2000; von Savigny et al., 2003; Arosio et al., 2019) in the time window 2003 – 2018. The tangent height of 41.3 km is selected due to its highest sensitivity to stratospheric ozone concentrations, which peaks about that altitude. Ozone is produced in the tropics and circulation patterns transport it poleward. It is usually located above the tropopause and its concentrations are higher during winter months and lowest in summer months. Despite its high variability through the year, total ozone trends are generally small in the order of $\pm$1%. Focusing on the Arctic, average total ozone is 353 DU and also exhibits a distinct maximum in spring months and a minimum in summer months. The Arctic-wide trend of total ozone is positive by 3.9 DU (+1.1%) decade^{-1}, in line with global values.

Greater significant positive trends, ranging from +4 to +10% decade^{-1}, are found in stratospheric ozone. They are centred above Greenland and stretch out along the 75°N parallel from the Greenland Sea through the Beaufort Sea in spring (AMJ) with a longer tongue over the Siberian Continent in summer (JAS). Contrasting the total with the stratospheric column yields the influence of the tropospheric ozone only. For those locations where the trend in total ozone is absent but positive in the stratosphere, a negative tropospheric trend can be deduced. This mechanism is consistently found above 70°N from the Canadian Archipelago through to the East Siberian Sea, irrespective of the season, together with the sustained positive trend above the Atlantic (the Greenland Sea), the neighbouring Barents Sea and the northern part of mainland Greenland (Gaudel et al., 2020). This reverses in a dipole fashion in JAS, when patterns of positive trends in total ozone are advected southward. In summary, when analysing R_λ^{TOA} trends at $\lambda = 620$ nm, and to a lesser extent 560 nm and 665 nm, changes in ozone contribute for those Arctic sectors affected by the meridional dynamics of air masses in which the stratospheric ozone is increasing. The most eastern Arctic sectors (East Siberian, Laptev and Kara Seas) have a smaller contribution from ozone changes than the western sectors. This is consistent with a neutral ozone trend observed over these areas.

Finally, we speculate that a surface warming of the Arctic might inflate the tropopause, inducing the production of polar stratospheric clouds as a result of colder temperatures. Lower ozone would absorb less UV and visible radiation, cooling the stratosphere further and potentially accelerating further its depletion. Albeit within natural variability, Turner et al. (2009) held stratospheric ozone depletion responsible for a change in wind flows and patterns across the South Pole, stimulating anti-correlated changes in sea ice extent of the Antarctic continent. This hypothesis could also be tested for the Arctic, using the results from this investigation.

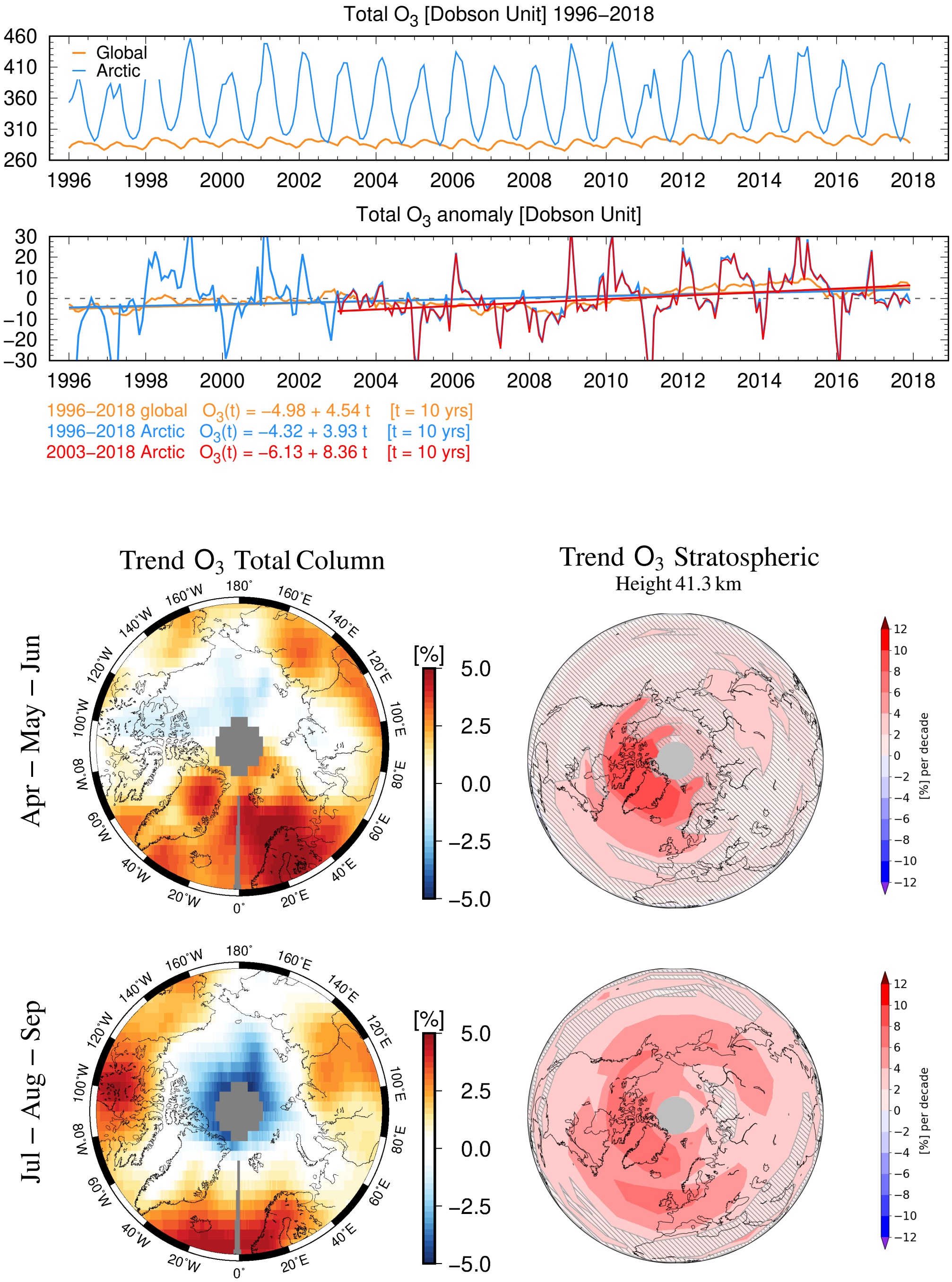

Figure A1. Top: global and Arctic record of total ozone with the respective anomalies and trends. The Arctic time series has been additionally shortened to match the length of the stratospheric ozone column. Bottom: trends (% decade^{-1}) of total (left) and stratospheric (right) ozone between 2003 and 2018 are plotted for spring (AMJ) and summer (JAS) months.

Table A1. List of abbreviations used in the main text.

Acronym	Meaning
AIRS	Atmospheric Infrared Sounder
ASTER	Advanced Spaceborne Thermal Emission and Reflection Radiometer
ATSR-2	Along Track Scanning Radiometer 2
AVHRR	Advanced Very-High-Resolution Radiometer
BRDF	Bidirectional Reflectance Distribution Function
BSRN	Baseline Surface Radiation Network
CALIPSO	Cloud-Aerosol Lidar and Infrared Pathfinder Satellite Observation
CALIOP	Cloud-Aerosol Lidar with Orthogonal Polarization
CERES	Clouds and the Earth's Radiant Energy System
DARDAR	raDAR liDAR combined cloud properties retrieval
EBAF	Energy balanced and filled
ENVISAT	Environmental Satellite
ERBE	Earth Radiation Budget Experiment
ERS-2	European Remote-Sensing Satellite 2
GOME	Global Ozone Monitoring Experiment
OMI	Ozone Measuring Instrument
MERIS	MEdium Resolution Imaging Spectrometer
MetOp	Meteorological Operational satellite
MODIS	Moderate Resolution Imaging Spectroradiometer
OMPS	Ozone Mapping and Profiler Suite
POES	Polar Operational Environmental Satellite
SBUV	Solar Backscatter Ultraviolet
SCIAMACHY	Scanning Imaging Absorption Spectrometer for Atmospheric Chartography
SeaWiFS	Sea-Viewing Wide Field-of-View Sensor
SHEBA	Surface Heat Budget of the Arctic Ocean
TIROS	Television Infrared Observation Satellite
TOMS	Total Ozone Mapping Spectrometer
TOVS	TIROS Operational Vertical Sounder

Table A2. Specifications of the instruments and data set versions selected for this work.[a]Full coverage until May 2003. [b]Payload switched-off since July 2011. [c]Lost contact on April 8, 2012. [d]Nominal end of GOME-2C record. [e]GOME-2A configuration change for tandem mode with GOME-2B on July 15, 2013. Foreseen extended lifetimes: November 2021 (GOME-2A), 2025 (GOME-2B), 2031 (GOME-2C).

	GOME	SCIAMACHY	GOME-2
Data availability	1996 – 2011[a,b]	2002 – 2012[c]	2007 – 2023[d,e]
Level 1 data processors	5.0	8.01	6.0
Equator crossing (LT)	10:30 AM	10:00 AM	9:30 AM
Global coverage [days]	3	6	1.5
Spectral coverage [nm]	237 – 794	240 – 2400	237 – 794
Spectral resolution [nm]	0.38	0.44	0.48
Pixel size at nadir [km^2]	320 × 40	60 × 30	80 × 40
Swath width [km]	960	1000	1920

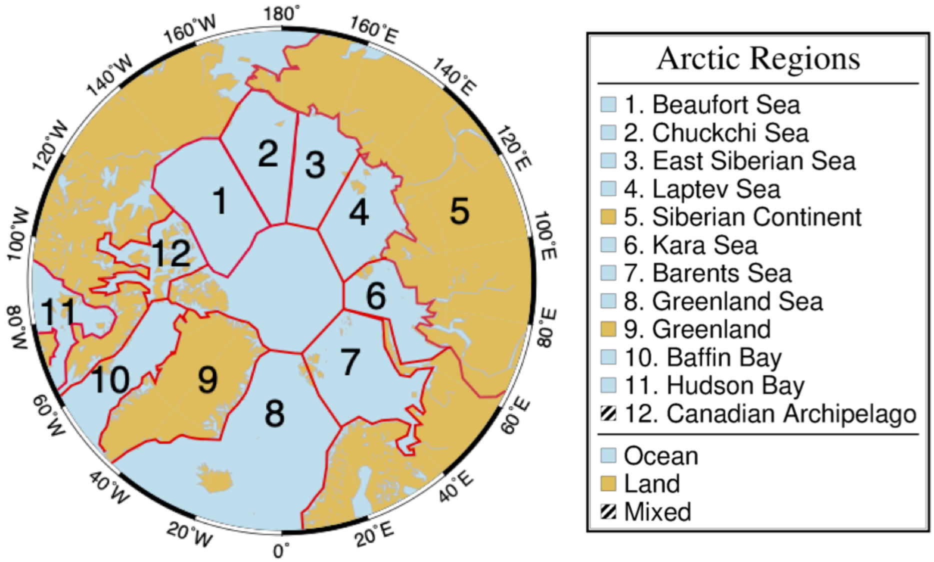

Figure B1. Definition of the Arctic climate zones, identified by distinct geophysical settings, that will be used in this study to derive local trends of R_λ^{TOA}, cloud properties and forcing. The geographical subdivision follows that of Serreze and Barry (2014) and Wang and Key (2005a).

Table B1. Multiyear seasonal means (± standard deviation) of cloud properties for the full Arctic and 12 regions of Fig. B1.

	Cloud cover Cloud albedo		Cloud height [km] r_{eff} [μm]		τ-liquid LWP [$\mathrm{g\,m^{-2}}$]		τ-ice IWP [$\mathrm{g\,m^{-2}}$]	
Region	AMJ	JAS	AMJ	JAS	AMJ	JAS	AMJ	JAS
Full Arctic	0.70 ± 0.12	0.76 ± 0.10	3.67 ± 0.57	4.14 ± 0.52	13.71 ± 5.75	14.21 ± 3.78	10.34 ± 3.86	12.05 ± 3.80
	0.52 ± 0.05	0.55 ± 0.06	11.87 ± 1.83	12.57 ± 1.43	126.21 ± 64.63	131.56 ± 41.14	148.08 ± 68.71	166.70 ± 73.02
1. Beaufort Sea	0.62 ± 0.19	0.80 ± 0.11	2.82 ± 0.62	3.33 ± 0.48	18.32 ± 8.43	12.71 ± 4.45	12.08 ± 3.67	9.90 ± 3.87
	0.60 ± 0.07	0.58 ± 0.07	10.89 ± 1.83	11.89 ± 1.62	171.35 ± 91.52	111.93 ± 50.43	179.45 ± 81.74	137.50 ± 79.72
2. Chuckchi Sea	0.68 ± 0.14	0.78 ± 0.10	3.30 ± 0.61	3.73 ± 0.50	15.69 ± 7.15	13.91 ± 4.00	10.63 ± 3.63	11.04 ± 3.80
	0.56 ± 0.06	0.58 ± 0.05	11.21 ± 1.91	11.97 ± 1.54	146.07 ± 85.95	123.31 ± 43.60	159.03 ± 73.16	151.06 ± 73.22
3. East Siberian Sea	0.68 ± 0.18	0.82 ± 0.09	2.94 ± 0.64	3.29 ± 0.48	17.43 ± 7.53	13.15 ± 4.13	11.77 ± 3.16	10.89 ± 3.85
	0.58 ± 0.06	0.58 ± 0.07	10.87 ± 1.91	11.96 ± 1.54	157.28 ± 79.00	112.23 ± 41.34	176.44 ± 65.94	153.52 ± 75.82
4. Laptev Sea	0.70 ± 0.18	0.83 ± 0.08	2.99 ± 0.61	3.34 ± 0.46	16.70 ± 7.37	14.77 ± 4.17	12.21 ± 3.34	12.07 ± 4.19
	0.59 ± 0.05	0.61 ± 0.06	10.37 ± 1.93	11.49 ± 1.54	145.73 ± 80.45	122.56 ± 41.38	179.37 ± 70.10	163.62 ± 81.67
5. Siberian Cont.	0.71 ± 0.10	0.74 ± 0.11	4.00 ± 0.55	4.47 ± 0.53	11.67 ± 5.00	15.02 ± 3.69	9.51 ± 4.28	13.02 ± 3.93
	0.47 ± 0.05	0.54 ± 0.06	12.31 ± 1.81	12.90 ± 1.34	106.21 ± 52.39	142.58 ± 40.23	136.00 ± 68.55	183.46 ± 74.40
6. Kara Sea	0.73 ± 0.16	0.82 ± 0.09	3.01 ± 0.62	3.39 ± 0.48	18.22 ± 7.77	16.69 ± 4.35	12.65 ± 3.72	12.80 ± 4.36
	0.59 ± 0.05	0.62 ± 0.05	10.08 ± 1.74	11.35 ± 1.55	151.44 ± 76.56	137.56 ± 38.87	187.25 ± 79.24	167.75 ± 79.36
7. Barents Sea	0.83 ± 0.10	0.84 ± 0.08	2.84 ± 0.47	3.38 ± 0.48	17.25 ± 4.68	17.46 ± 3.77	11.57 ± 3.65	13.31 ± 3.99
	0.59 ± 0.04	0.63 ± 0.04	10.96 ± 1.33	11.81 ± 1.67	141.73 ± 47.12	149.59 ± 36.13	152.60 ± 65.12	170.17 ± 72.77
8. Greenland Sea	0.84 ± 0.07	0.85 ± 0.06	3.18 ± 0.51	3.76 ± 0.59	14.53 ± 3.41	15.65 ± 3.30	10.81 ± 3.16	12.84 ± 3.60
	0.54 ± 0.05	0.58 ± 0.04	12.70 ± 1.31	13.23 ± 1.53	131.02 ± 34.18	147.43 ± 35.89	136.48 ± 51.25	165.13 ± 67.43
9. Greenland	0.51 ± 0.12	0.63 ± 0.11	5.32 ± 0.62	5.42 ± 0.46	8.40 ± 7.33	6.73 ± 3.47	5.97 ± 1.83	5.98 ± 1.83
	0.47 ± 0.05	0.48 ± 0.06	11.23 ± 2.42	11.30 ± 1.55	104.76 ± 134.88	73.46 ± 51.65	99.66 ± 44.58	93.83 ± 36.57
10. Baffin Bay	0.75 ± 0.12	0.78 ± 0.09	3.27 ± 0.60	3.88 ± 0.61	14.65 ± 5.29	13.36 ± 2.98	10.29 ± 3.41	11.64 ± 3.69
	0.52 ± 0.05	0.55 ± 0.05	11.55 ± 1.57	12.94 ± 1.41	129.63 ± 53.41	124.53 ± 32.97	144.34 ± 58.54	157.37 ± 68.47
11. Hudson Bay	0.73 ± 0.12	0.70 ± 0.13	3.33 ± 0.70	4.40 ± 0.64	12.93 ± 5.91	13.04 ± 3.42	9.61 ± 3.82	12.49 ± 4.52
	0.45 ± 0.06	0.51 ± 0.06	11.26 ± 1.84	13.41 ± 1.32	115.37 ± 57.56	123.51 ± 37.05	139.26 ± 62.42	176.42 ± 85.70
12. Canadian Arch.	0.65 ± 0.15	0.78 ± 0.12	3.15 ± 0.69	3.57 ± 0.55	17.24 ± 8.76	13.51 ± 4.15	11.98 ± 4.49	11.44 ± 3.97
	0.57 ± 0.07	0.57 ± 0.06	11.55 ± 1.98	12.52 ± 1.32	174.23 ± 107.76	123.08 ± 46.81	204.37 ± 105.59	162.03 ± 82.11

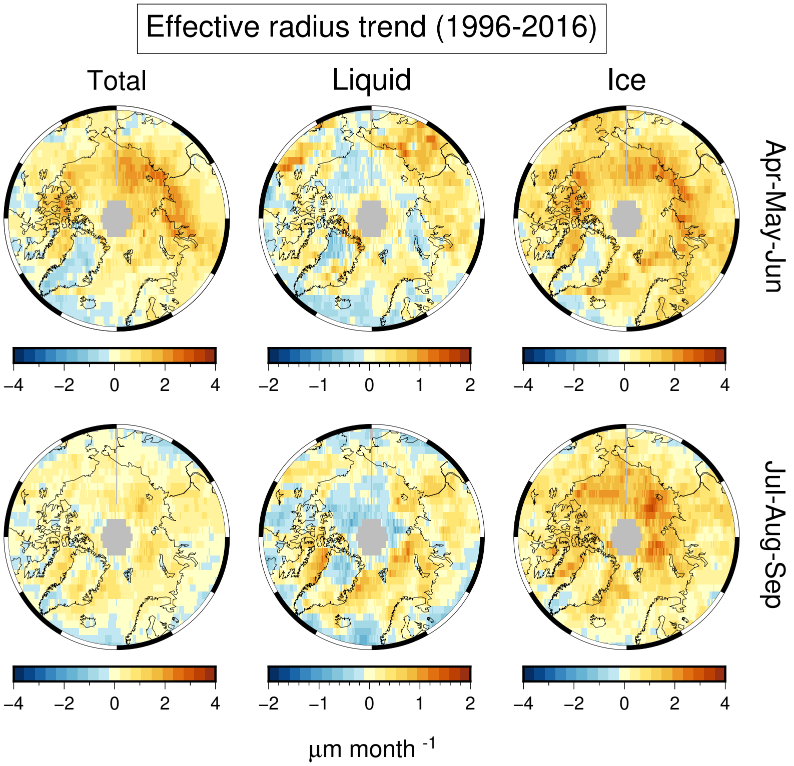

Figure C1. Seasonal trends (top: Apr-May-Jun; bottom: Jul-Aug-Sep) of cloud effective radius (in μm month^{-1}) for total cloud (left), liquid only (center) and ice only (right) thermodynamic phase. These values are representative of trends for either liquid droplets or ice crystals located at ≈ 1-τ depth from the cloud top.

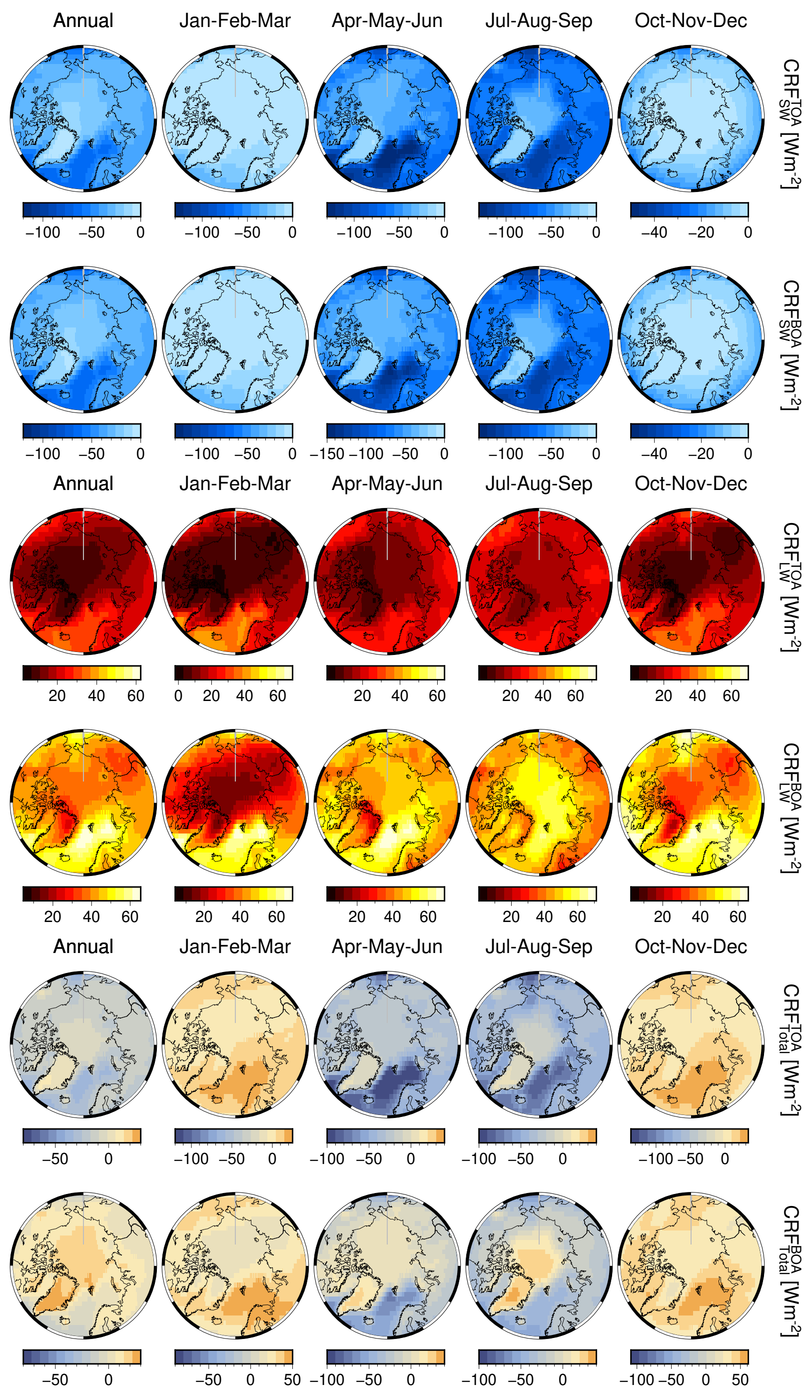

Figure D1. From left to right, annual and seasonal average values of SW (rows 1-2), LW (3-4) and total (5-6) cloud radiative forcing (CRF, W m^{-2}) at TOA and BOA, respectively. Note the different color scales to match the CRF ranges.

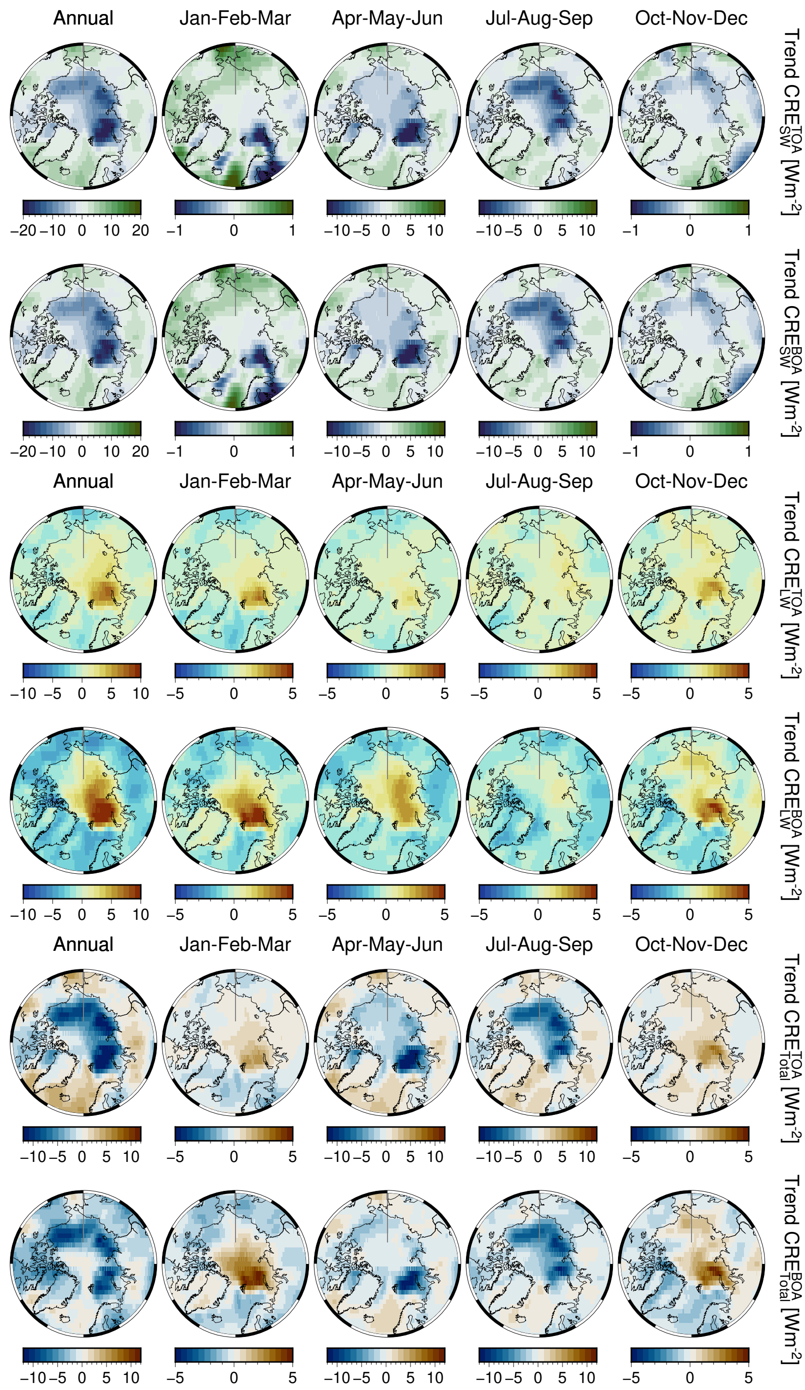

Figure D2. From left to right, annual and seasonal trends of SW (rows 1-2), LW (3-4) and total (5-6) cloud radiative effect (CRE, W m^{-2}) at TOA and BOA.

Author contributions. L.L., M.V., J-P.B conceived the research. L.L. led code development, processed orbital reflectance data, analyzed all records and wrote the manuscript. N.K., M.V. processed orbital reflectance data and analyzed the record. Funding acquisition by L.L., M.V. and J-P.B. All authors contributed to the interpretation of the results and the final drafting of the paper.

Competing interests. The authors declare that they have no competing interests.

Code availability. Perl and Bash code to extract, harmonize, grid and analyze all data records is available from the first author upon request. Essential software such as Generic Mapping Tools (GMT) and Climate Data Operators (CDO) is available at the respective websites.

Data availability. Native L1 orbital data (versioned with total size) of spectral reflectance are available at https://earth.esa.int/eogateway/catalog/ for GOME (v5.1, 2.47 TB), SCIAMACHY (v9.01, 16.98 TB) and MERIS (v8, 23.75 TB in Reduced Resolution). GOME-2A/B (v5.3 until June 2014, v6.x afterward, 58.28 TB each) have been accessed via EumetCast. We recommend users to download the newly reprocessed GOME-2 Fundamental Data Record (FDR) v3 available at http://doi.org/10.15770/EUM_SEC_CLM_0039. The Arctic spectral subset (10 wavelengths bands north of the 60°latitude, ≈13 TB) of L1 orbital data is available upon request. Due to obvious size limitations, we have prepared a monthly spectral reflectance data set available at https://doi.pangaea.de/10.1594/PANGAEA.933905. Cloud and flux data are available at the DWD website https://doi.org/10.5676/DWD/ESA_Cloud_cci/AVHRR-PM/V003.

Acknowledgements. We thank Kamesh Vinjamuri (IUP Bremen) for validation of AVHRR radiance and cloud optical properties; Carlo Arosio (IUP Bremen) for provision of stratospheric ozone data; Alessandra Cacciari (EUMETSAT) for the intepretation of GOME-2A sensing geometry. ESA Cloud CCI working group for the processing the AVHRR data set. For valuable discussions we acknowledge Ann Fridlind (NASA/GISS), Tido Semmler, Felix Pithan (AWI Bremerhaven) and especially Kerstin Ebell (Uni Cologne). This work has been funded by the Deutsche Forschungsgemeinschaft (DFG, German Research Foundation) within the project "ArctiC Amplification: Climate Relevant Atmospheric and SurfaCe Processes, and Feedback Mechanisms $(AC)^3$" as Transregional Collaborative Research Center (TRR) 172, Project-ID 268020496. Luca Lelli, as visiting scientist within the NASA/Goddard Space Flight Center PACE (Plankton, Aerosol, Cloud, ocean Ecosystem) project, ~~is~~ was supported by the Alexander von Humboldt Foundation through the Feodor-Lynen Fellowship 2020. Prof. Zhanqing Li (UMD - University of Maryland), Jeremy Werdell (OEL - Ocean Ecology Laboratory, NASA/GSFC) and Andrew Sayer (NASA/GSFC and USRA - Universities Space Research Association) have been instrumental in the establishment of this cooperation. Luca Lelli thanks Theofanis Stamoulis for the initial steps with reflectances, which eventually evolved in this paper.

References

Arosio, C., Rozanov, A., Malinina, E., Weber, M., and Burrows, J. P.: Merging of ozone profiles from SCIAMACHY, OMPS and SAGE II observations to study stratospheric ozone changes, Atmospheric Measurement Techniques, 12, 2423–2444, https://doi.org/10.5194/amt-12-2423-2019, 2019.

Arrhenius, S.: On the influence of carbonic acid in the air upon the temperature of the ground, The London, Edinburgh, and Dublin Philosophical Magazine and Journal of Science, 41, 237–276, https://www.rsc.org/images/Arrhenius1896_tcm18-173546.pdf, 1896.

Baldridge, A., Hook, S., Grove, C., and Rivera, G.: The ASTER spectral library version 2.0, Remote Sensing of Environment, 113, 711 – 715, https://doi.org/10.1016/j.rse.2008.11.007, 2009.

Bennartz, R., Shupe, M., Turner, D., Walden, V., Steffen K., Cox, C., Kulie, M., Miller, N., and Pettersen, C.: Greenland melt extent enhanced by low-level liquid clouds, Nature, https://doi.org/10.1038/nature12002, 2013.

Bjordal, J., Storelvmo, T., Alterskjær, K., and Carlsen, T.: Equilibrium climate sensitivity above 5 C plausible due to state-dependent cloud feedback, Nature Geoscience, 13, 718–721, https://doi.org/10.1038/s41561-020-00649-1, 2020.

Boccolari, M. and Parmiggiani, F.: Trends and variability of cloud fraction cover in the Arctic, 1982–2009, Theoretical and Applied Climatology, 132, 739–749, https://doi.org/10.1007/s00704-017-2125-6, 2018.

Boisvert, L. N. and Stroeve, J. C.: The Arctic is becoming warmer and wetter as revealed by the Atmospheric Infrared Sounder, Geophysical Research Letters, 42, 4439–4446, https://doi.org/10.1002/2015GL063775, 2015.

Burrows, J., Hölzle, E., Goede, A., Visser, H., and Fricker, W.: SCIAMACHY, Scanning Imaging Absorption spectroMeter for Atmospheric CHartographY, Acta Astronautica, 35, 445 – 451, https://doi.org/10.1016/0094-5765(94)00278-T, 1995.

Burrows, J. P., Weber, M., Buchwitz, M., Rozanov, V., Ladstätter-Weissenmayer, A., Richter, A., DeBeek, R., Hoogen, R., Bramstedt, K., Eichmann, K.-U., Eisinger, M., and Perner, D.: The Global Ozone Monitoring Experiment (GOME): Mission Concept and First Scientific Results, Journal of the Atmospheric Sciences, 56, 151–175, https://doi.org/10.1175/1520-0469(1999)056<0151:TGOMEG>2.0.CO;2, 1999.

Cannon, A. J.: Defining climatological seasons using radially constrained clustering, Geophysical Research Letters, 32, https://doi.org/10.1029/2005GL023410, 2005.

Ceppi, P., McCoy, D. T., and Hartmann, D. L.: Observational evidence for a negative shortwave cloud feedback in middle to high latitudes, Geophysical Research Letters, 43, 1331–1339, https://doi.org/10.1002/2015GL067499, 2016.

Cesana, G. and Storelvmo, T.: Improving climate projections by understanding how cloud phase affects radiation, Journal of Geophysical Research: Atmospheres, 122, 4594–4599, https://doi.org/10.1002/2017JD026927, 2017.

Chan, M. A. and Comiso, J. C.: Arctic Cloud Characteristics as Derived from MODIS, CALIPSO, and CloudSat, Journal of Climate, 26, 3285–3306, https://doi.org/10.1175/JCLI-D-12-00204.1, 2013.

Christensen, M., Poulsen, C., McGarragh, G., and Grainger, R.: Algorithm Theoretical Basis Document (ATBD) of the Community Code for CLimate (CC4CL) Broadband Radiative Flux Retrieval (CC4CL-TOAFLUX) module - Cloud_CCI Working Group, Tech. rep., European Space Agency, https://climate.esa.int/media/documents/Cloud_Algorithm-Theoretical-Baseline-Document-ATBD-CC4CL-TOAFLUX_v1.1.pdf, last access July 2019, 2016.

Clementson, L. A. and Wojtasiewicz, B.: Dataset on the absorption characteristics of extracted phytoplankton pigments, Data in Brief, 24, 103 875, https://doi.org/10.1016/j.dib.2019.103875, 2019.

Cloud_CCI Working Group: Product Validation and Intercomparison Report (PVIR), Tech. rep., European Space Agency, https://climate.esa.int/media/documents/Cloud_Product-Validation-and-Intercomparison-Report-PVIR_v6.0.pdf, last access July 2020, 2020.

Coldewey-Egbers, M., Weber, M., Lamsal, L. N., de Beek, R., Buchwitz, M., and Burrows, J. P.: Total ozone retrieval from GOME UV spectral data using the weighting function DOAS approach, Atmospheric Chemistry and Physics, 5, 1015–1025, https://doi.org/10.5194/acp-5-1015-2005, 2005.

Crook, J. A., Forster, P. M., and Stuber, N.: Spatial patterns of modeled climate feedback and contributions to temperature response and polar amplification, Journal of Climate, 24, 3575–3592, https://doi.org/10.1175/2011JCLI3863.1, 2011.

Curry, J. A., Schramm, J. L., Rossow, W. B., and Randall, D.: Overview of Arctic Cloud and Radiation Characteristics, Journal of Climate, 9, 1731 – 1764, https://doi.org/10.1175/1520-0442(1996)009<1731:OOACAR>2.0.CO;2, 1996.

Delanoë, J. and Hogan, R. J.: Combined CloudSat-CALIPSO-MODIS retrievals of the properties of ice clouds, Journal of Geophysical Research: Atmospheres, 115, https://doi.org/10.1029/2009JD012346, 2010.

Donohoe, A. and Battisti, D. S.: Atmospheric and Surface Contributions to Planetary Albedo, Journal of Climate, 24, 4402–4418, https://doi.org/10.1175/2011JCLI3946.1, 2011.

Eastman, R. and Warren, S. G.: Interannual Variations of Arctic Cloud Types in Relation to Sea Ice, Journal of Climate, 23, 4216–4232, https://doi.org/10.1175/2010JCLI3492.1, 2010a.

Eastman, R. and Warren, S. G.: Arctic Cloud Changes from Surface and Satellite Observations, Journal of Climate, 23, 4233–4242, https://doi.org/10.1175/2010JCLI3544.1, 2010b.

Ebell, K., Nomokonova, T., Maturilli, M., and Ritter, C.: Radiative Effect of Clouds at Ny-Ålesund, Svalbard, as Inferred from Ground-Based Remote Sensing Observations, Journal of Applied Meteorology and Climatology, 59, 3–22, https://doi.org/10.1175/JAMC-D-19-0080.1, 2019.

Efron, B. and Tibshirani, R. J.: An Introduction to the Bootstrap, Chapman & Hall, New York, https://doi.org/10.1201/9780429246593, 1993.

Fasullo, J. and Webster, P. J.: A Hydrological Definition of Indian Monsoon Onset and Withdrawal, Journal of Climate, 16, 3200 – 3211, https://doi.org/10.1175/1520-0442(2003)016<3200a:AHDOIM>2.0.CO;2, 2003.

Fazel-Rastgar, F.: Seasonal Analysis of Atmospheric Changes in Hudson Bay during 1998-2018, American Journal of Climate Change, 9, 100, https://doi.org/10.4236/ajcc.2020.92008, 2020.

Flittner, D. E., Bhartia, P. K., and Herman, B. M.: O_3 profiles retrieved from limb scatter measurements: Theory, Geophysical Research Letters, 27, 2601–2604, https://doi.org/10.1029/1999GL011343, 2000.

Francis, J. A. and Hunter, E.: New insight into the disappearing Arctic sea ice, Eos, Transactions American Geophysical Union, 87, 509–511, https://doi.org/10.1029/2006EO460001, 2006.

Frey, K. E., Comiso, J., Cooper, L. W., Grebmeier, J. M., and Stock, L. V.: Arctic Ocean primary productivity: The response of marine algae to climate warming and sea ice decline, in: Arctic Report Card, vol. 100, NOAA, https://www.arctic.noaa.gov/Report-Card, 2018.

Fu, Q. and Liou, K. N.: On the Correlated k-Distribution Method for Radiative Transfer in Nonhomogeneous Atmospheres, Journal of Atmospheric Sciences, 49, 2139 – 2156, https://doi.org/10.1175/1520-0469(1992)049<2139:OTCDMF>2.0.CO;2, 1992.

Gaudel, A., Cooper, O. R., Chang, K.-L., Bourgeois, I., Ziemke, J. R., Strode, S. A., Oman, L. D., Sellitto, P., Nédélec, P., Blot, R., Thouret, V., and Granier, C.: Aircraft observations since the 1990s reveal increases of tropospheric ozone at multiple locations across the Northern Hemisphere, Science Advances, 6, https://doi.org/10.1126/sciadv.aba8272, 2020.

Gettelman, A. and Sherwood, S.: Processes responsible for cloud feedback, Current climate change reports, 2, 179–189, https://doi.org/10.1007/s40641-016-0052-8, 2016.

Gettelman, A., Hannay, C., Bacmeister, J. T., Neale, R. B., Pendergrass, A. G., Danabasoglu, G., Lamarque, J.-F., Fasullo, J. T., Bailey, D. A., Lawrence, D. M., and Mills, M. J.: High Climate Sensitivity in the Community Earth System Model Version 2 (CESM2), Geophysical Research Letters, 46, 8329–8337, https://doi.org/10.1029/2019GL083978, 2019.

Goosse, H., Kay, J. E., Armour, K. C., Bodas-Salcedo, A., Chepfer, H., Docquier, D., Jonko, A., Kushner, P. J., Lecomte, O., Massonnet, F., et al.: Quantifying climate feedbacks in polar regions, Nature communications, 9, 1–13, https://doi.org/10.1038/s41467-018-04173-0, 2018.

Gorshelev, V., Serdyuchenko, A., Weber, M., Chehade, W., and Burrows, J. P.: High spectral resolution ozone absorption cross-sections. Part 1: Measurements, data analysis and comparison with previous measurements around 293 K, Atmospheric Measurement Techniques, 7, 609–624, https://doi.org/10.5194/amt-7-609-2014, 2014.

Graßl, S. and Ritter, C.: Properties of Arctic Aerosol Based on Sun Photometer Long-Term Measurements in Ny-Ålesund, Svalbard, Remote Sensing, 11, https://doi.org/10.3390/rs11111362, 2019.

Grosvenor, D. P., Sourdeval, O., Zuidema, P., Ackerman, A., Alexandrov, M. D., Bennartz, R., Boers, R., Cairns, B., Chiu, J. C., Christensen, M., et al.: Remote sensing of droplet number concentration in warm clouds: A review of the current state of knowledge and perspectives, Reviews of Geophysics, 56, 409–453, https://doi.org/10.1029/2017RG000593, 2018.

Guarino, M.-V., Sime, L. C., Schröeder, D., Malmierca-Vallet, I., Rosenblum, E., Ringer, M., Ridley, J., Feltham, D., Bitz, C., Steig, E. J., et al.: Sea-ice-free Arctic during the Last Interglacial supports fast future loss, Nature Climate Change, 10, 928–932, https://doi.org/10.1038/s41558-020-0865-2, 2020.

He, M., Hu, Y., Chen, N., Wang, D., Huang, J., and Stamnes, K.: High cloud coverage over melted areas dominates the impact of clouds on the albedo feedback in the Arctic, Scientific Reports, 9, https://doi.org/10.1038/s41598-019-44155-w, 2019.

Henderson, D. S., L‚ÄôEcuyer, T., Stephens, G., Partain, P., and Sekiguchi, M.: A Multisensor Perspective on the Radiative Impacts of Clouds and Aerosols, Journal of Applied Meteorology and Climatology, 52, 853 – 871, https://doi.org/10.1175/JAMC-D-12-025.1, 2013.

Herman, G. and Goody, R.: Formation and persistence of summertime Arctic stratus clouds, Journal of the Atmospheric Sciences, 33, 1537–1553, https://doi.org/10.1175/1520-0469(1976)033<1537:FAPOSA>2.0.CO;2, 1976.

Hersbach, H., Bell, B., Berrisford, P., Hirahara, S., Horányi, A., Muñoz-Sabater, J., Nicolas, J., Peubey, C., Radu, R., Schepers, D., Simmons, A., Soci, C., Abdalla, S., Abellan, X., Balsamo, G., Bechtold, P., Biavati, G., Bidlot, J., Bonavita, M., De Chiara, G., Dahlgren, P., Dee, D., Diamantakis, M., Dragani, R., Flemming, J., Forbes, R., Fuentes, M., Geer, A., Haimberger, L., Healy, S., Hogan, R. J., Hólm, E., Janisková, M., Keeley, S., Laloyaux, P., Lopez, P., Lupu, C., Radnoti, G., de Rosnay, P., Rozum, I., Vamborg, F., Villaume, S., and Thépaut, J.-N.: The ERA5 global reanalysis, Quarterly Journal of the Royal Meteorological Society, 146, 1999–2049, https://doi.org/10.1002/qj.3803, 2020.

Heslin-Rees, D., Burgos, M., Hansson, H.-C., Krejci, R., Ström, J., Tunved, P., and Zieger, P.: From a polar to a marine environment: has the changing Arctic led to a shift in aerosol light scattering properties?, Atmospheric Chemistry and Physics, 20, 13 671–13 686, https://doi.org/10.5194/acp-20-13671-2020, 2020.

Hilboll, A., Richter, A., and Burrows, J. P.: Long-term changes of tropospheric NO_2 over megacities derived from multiple satellite instruments, Atmospheric Chemistry and Physics, 13, 4145–4169, https://doi.org/10.5194/acp-13-4145-2013, 2013.

Hofer, S., Tedstone, A. J., Fettweis, X., and Bamber, J. L.: Decreasing cloud cover drives the recent mass loss on the Greenland Ice Sheet, Science Advances, 3, https://doi.org/10.1126/sciadv.1700584, 2017.

Hofer, S., Tedstone, A. J., Fettweis, X., and Bamber, J. L.: Cloud microphysics and circulation anomalies control differences in future Greenland melt, Nature Climate Change, 9, 523–528, https://doi.org/10.1038/s41558-019-0507-8, 2019.

Holland, M. M., Bitz, C. M., Tremblay, B., Bailey, D. A., et al.: The role of natural versus forced change in future rapid summer Arctic ice loss, Arctic Sea Ice Decline: Observations, Projections, Mechanisms, and Implications, Geophys. Monogr. Ser, 180, 133–150, https://doi.org/10.1029/180GM10, 2008.

Huang, Y., Dong, X., Kay, J. E., Xi, B., and McIlhattan, E. A.: The climate response to increased cloud liquid water over the Arctic in CESM1: a sensitivity study of Wegener–Bergeron–Findeisen process, Climate Dynamics, 56, 3373–3394, https://doi.org/10.1007/s00382-021-05648-5, 2021.

Intrieri, J. M., Fairall, C. W., Shupe, M. D., Persson, P. O. G., Andreas, E. L., Guest, P. S., and Moritz, R. E.: An annual cycle of Arctic surface cloud forcing at SHEBA, Journal of Geophysical Research: Oceans, 107, SHE 13–1–SHE 13–14, https://doi.org/10.1029/2000JC000439, 2002.

Istomina, L., Nicolaus, M., and Perovich, D. K.: Spectral albedo of sea ice and melt ponds measured during POLARSTERN cruise ARK-XXVII/3 (IceArc) in 2012, https://doi.org/10.1594/PANGAEA.815111, 2013.

Jones, P. W.: First-and second-order conservative remapping schemes for grids in spherical coordinates, Monthly Weather Review, 127, 2204–2210, https://doi.org/10.1175/1520-0493(1999)127<2204:FASOCR>2.0.CO;2, 1999.

Kapsch, M.-L., Graversen, R. G., and Tjernström, M.: Springtime atmospheric energy transport and the control of Arctic summer sea-ice extent, Nature Climate Change, 3, 744–748, https://doi.org/10.1038/NCLIMATE1884, 2013.

Karlsson, K.-G. and Devasthale, A.: Inter-comparison and evaluation of the four longest satellite-derived cloud climate data records: CLARA-A2, ESA Cloud CCI V3, ISCCP-HGM, and PATMOS-x, Remote Sensing, 10, 1567, https://doi.org/10.3390/rs10101567, 2018.

Kato, S., Loeb, N. G., Rose, F. G., Doelling, D. R., Rutan, D. A., Caldwell, T. E., Yu, L., and Weller, R. A.: Surface Irradiances Consistent with CERES-Derived Top-of-Atmosphere Shortwave and Longwave Irradiances, Journal of Climate, 26, 2719 – 2740, https://doi.org/10.1175/JCLI-D-12-00436.1, 2013.

Kay, J. E. and L'Ecuyer, T.: Observational constraints on Arctic Ocean clouds and radiative fluxes during the early 21st century, Journal of Geophysical Research: Atmospheres, 118, 7219–7236, https://doi.org/10.1002/jgrd.50489, 2013.

Keeling, C. D.: The concentration and isotopic abundances of atmospheric carbon dioxide in rural areas, Geochimica et Cosmochimica Acta, 13, 322–334, https://doi.org/10.1016/0016-7037(58)90033-4, 1958.

Keeling, C. D.: The Concentration and Isotopic Abundances of Carbon Dioxide in the Atmosphere, Tellus, 12, 200–203, https://doi.org/10.3402/tellusa.v12i2.9366, 1960.

Keeling, C. D., Bacastow, R. B., Bainbridge, A. E., Jr., C. A. E., Guenther, P. R., Waterman, L. S., and Chin, J. F. S.: Atmospheric carbon dioxide variations at Mauna Loa Observatory, Hawaii, Tellus, 28, 538–551, https://doi.org/10.3402/tellusa.v28i6.11322, 1976.

King, N. and Vaughan, G.: Using passive remote sensing to retrieve the vertical variation of cloud droplet size in marine stratocumulus: An assessment of information content and the potential for improved retrievals from hyperspectral measurements, Journal of Geophysical Research: Atmospheres, 117, https://doi.org/10.1029/2012JD017896, 2012.

Kokhanovsky, A. and Rozanov, V. V.: Droplet vertical sizing in warm clouds using passive optical measurements from a satellite, Atmospheric Measurement Techniques, 5, 517–528, https://doi.org/10.5194/amt-5-517-2012, 2012.

Kokhanovsky, A. and Tomasi, C.: Physics and Chemistry of the Arctic Atmosphere, Springer, https://doi.org/10.1007/978-3-030-33566-3, 2020.

Krijger, J. M., van Weele, M., Aben, I., and Frey, R.: Technical Note: The effect of sensor resolution on the number of cloud-free observations from space, Atmospheric Chemistry and Physics, 7, 2881–2891, https://doi.org/10.5194/acp-7-2881-2007, 2007.

Lelli, L. and Vountas, M.: Chapter 5 - Aerosol and Cloud Bottom Altitude Covariations From Multisensor Spaceborne Measurements, in: Remote Sensing of Aerosols, Clouds, and Precipitation, edited by Islam, T., Hu, Y., Kokhanovsky, A., and Wang, J., pp. 109–127, Elsevier, https://doi.org/10.1016/B978-0-12-810437-8.00005-0, 2018.

Lelli, L., Kokhanovsky, A. A., Rozanov, V. V., Vountas, M., Sayer, A. M., and Burrows, J. P.: Seven years of global retrieval of cloud properties using space-borne data of GOME, Atmospheric Measurement Techniques, 5, 1551–1570, https://doi.org/10.5194/amt-5-1551-2012, 2012.

Lelli, L., Kokhanovsky, A. A., Rozanov, V. V., Vountas, M., and Burrows, J. P.: Linear trends in cloud top height from passive observations in the oxygen A-band, Atmospheric Chemistry and Physics, 14, 5679–5692, https://doi.org/10.5194/acp-14-5679-2014, 2014.

Letterly, A., Key, J., and Liu, Y.: Arctic climate: changes in sea ice extent outweigh changes in snow cover, The Cryosphere, 12, 3373–3382, https://doi.org/10.5194/tc-12-3373-2018, 2018.

Li, Z. and Leighton, H. G.: Scene identification and its effect on cloud radiative forcing in the Arctic, Journal of Geophysical Research: Atmospheres, 96, 9175–9188, https://doi.org/10.1029/91JD00529, 1991.

Lindsay, R. and Zhang, J.: The thinning of Arctic sea ice, 1988–2003: Have we passed a tipping point?, Journal of Climate, 18, 4879–4894, https://doi.org/10.1175/JCLI3587.1, 2005.

Linlu, M., Burrows, J. P., Zhao, X., Vountas, M., Rozanov, V., Lelli, L., Li, X., Guo, H., Nakoudi, K., Ritter, C., and Edebor, A. A.: An analysis of AOT above the ocean in the Arctic observed from space: a reducing trend from 1981 to 2020, to be submitted, 2021.

Lohmann, U.: A glaciation indirect aerosol effect caused by soot aerosols, Geophysical Research Letters, 29, 11–1–11–4, https://doi.org/10.1029/2001GL014357, 2002.

Lohmann, U., Tselioudis, G., and Tyler, C.: Why is the cloud albedo–particle size relationship different in optically thick and optically thin clouds?, Geophysical research letters, 27, 1099–1102, https://doi.org/10.1029/1999GL011098, 2000.

Matus, A. V. and L'Ecuyer, T. S.: The role of cloud phase in Earth's radiation budget, Journal of Geophysical Research: Atmospheres, 122, 2559–2578, https://doi.org/10.1002/2016JD025951, 2017.

McCrystall, M. R., Stroeve, J., Serreze, M., Forbes, B. C., and Screen, J. A.: New climate models reveal faster and larger increases in Arctic precipitation than previously projected, Nature Communications, 12, 1–12, https://doi.org/10.1038/s41467-021-27031-y, 2021.

McGarragh, G. R., Poulsen, C. A., Thomas, G. E., Povey, A. C., Sus, O., Stapelberg, S., Schlundt, C., Proud, S., Christensen, M. W., Stengel, M., Hollmann, R., and Grainger, R. G.: The Community Cloud retrieval for CLimate (CC4CL) – Part 2: The optimal estimation approach, Atmospheric Measurement Techniques, 11, 3397–3431, https://doi.org/10.5194/amt-11-3397-2018, 2018.

McIlhattan, E. A., Kay, J. E., and L'Ecuyer, T. S.: Arctic Clouds and Precipitation in the Community Earth System Model Version 2, Journal of Geophysical Research: Atmospheres, 125, e2020JD032 521, https://doi.org/10.1029/2020JD032521, e2020JD032521 10.1029/2020JD032521, 2020.

Meerdink, S. K., Hook, S. J., Roberts, D. A., and Abbott, E. A.: The ECOSTRESS spectral library version 1.0, Remote Sensing of Environment, 230, 111 196, https://doi.org/10.1016/j.rse.2019.05.015, 2019.

Meerkötter, R. and Zinner, T.: Satellite remote sensing of cloud base height for convective cloud fields: A case study, Geophysical Research Letters, 34, https://doi.org/10.1029/2007GL030347, 2007.

Merk, D., Deneke, H., Pospichal, B., and Seifert, P.: Investigation of the adiabatic assumption for estimating cloud micro- and macrophysical properties from satellite and ground observations, Atmospheric Chemistry and Physics, 16, 933–952, https://doi.org/10.5194/acp-16-933-2016, 2016.

Mieruch, S.: Identification and statistical analysis of global water vapour trends based on satellite data, Ph.D. thesis, University of Bremen, http://nbn-resolving.de/urn:nbn:de:gbv:46-diss000115889, 2009.

Mioche, G., Jourdan, O., Delanoë, J., Gourbeyre, C., Febvre, G., Dupuy, R., Monier, M., Szczap, F., Schwarzenboeck, A., and Gayet, J.-F.: Vertical distribution of microphysical properties of Arctic springtime low-level mixed-phase clouds over the Greenland and Norwegian seas, Atmospheric Chemistry and Physics, 17, 12 845–12 869, https://doi.org/10.5194/acp-17-12845-2017, 2017.

Morrison, A. L., Kay, J. E., Chepfer, H., Guzman, R., and Yettella, V.: Isolating the Liquid Cloud Response to Recent Arctic Sea Ice Variability Using Spaceborne Lidar Observations, Journal of Geophysical Research: Atmospheres, 123, 473–490, https://doi.org/10.1002/2017JD027248, 2018.

Morrison, A. L., Kay, J. E., Frey, W. R., Chepfer, H., and Guzman, R.: Cloud Response to Arctic Sea Ice Loss and Implications for Future Feedback in the CESM1 Climate Model, Journal of Geophysical Research: Atmospheres, 124, 1003–1020, https://doi.org/10.1029/2018JD029142, 2019.

Mudelsee, M.: Climate Time Series Analysis: Classical Statistical and Bootstrap Methods, Atmospheric and Oceanographic Sciences Library, Vol. 42, Springer, Dordrecht Heidelberg London New York, https://doi.org/10.1007/978-90-481-9482-7, 2010.

Munro, R., Lang, R., Klaes, D., Poli, G., Retscher, C., Lindstrot, R., Huckle, R., Lacan, A., Grzegorski, M., Holdak, A., Kokhanovsky, A., Livschitz, J., and Eisinger, M.: The GOME-2 instrument on the Metop series of satellites: instrument design, calibration, and level 1 data processing – an overview, Atmospheric Measurement Techniques, 9, 1279–1301, https://doi.org/10.5194/amt-9-1279-2016, 2016.

Notz, D. and Community, S.: Arctic Sea Ice in CMIP6, Geophysical Research Letters, 47, e2019GL086 749, https://doi.org/10.1029/2019GL086749, e2019GL086749 10.1029/2019GL086749, 2020.

Onarheim, I. H., Eldevik, T., Smedsrud, L. H., and Stroeve, J. C.: Seasonal and regional manifestation of Arctic sea ice loss, Journal of Climate, 31, 4917–4932, https://doi.org/10.1175/JCLI-D-17-0427.1, 2018.

Philipp, D., Stengel, M., and Ahrens, B.: Analyzing the Arctic Feedback Mechanism between Sea Ice and Low-Level Clouds Using 34 Years of Satellite Observation, Journal of Climate, 33, 7479 – 7501, https://doi.org/10.1175/JCLI-D-19-0895.1, 2020.

Pistone, K., Eisenman, I., and Ramanathan, V.: Observational determination of albedo decrease caused by vanishing Arctic sea ice, Proceedings of the National Academy of Sciences, 111, 3322–3326, https://doi.org/10.1073/pnas.1318201111, 2014.

Pithan, F. and Mauritsen, T.: Arctic amplification dominated by temperature feedbacks in contemporary climate models, Nature Geoscience, 7, 181, https://doi.org/10.1038/ngeo2071, 2014.

Platnick, S.: Vertical photon transport in cloud remote sensing problems, Journal of Geophysical Research: Atmospheres, 105, 22 919–22 935, https://doi.org/10.1029/2000JD900333, 2000.

Rinke, A., Segger, B., Crewell, S., Maturilli, M., Naakka, T., Nygård, T., Vihma, T., Alshawaf, F., Dick, G., Wickert, J., et al.: Trends of vertically integrated water vapor over the Arctic during 1979–2016: Consistent moistening all over?, Journal of Climate, 32, 6097–6116, https://doi.org/10.1175/JCLI-D-19-0092.1, 2019.

Rodhe, H., Charlson, R., and Crawford, E.: Svante Arrhenius and the Greenhouse Effect, Ambio, 26, 2–5, http://www.jstor.org/stable/4314542, 1997.

Rozanov, V. V. and Kokhanovsky, A. A.: Semianalytical cloud retrieval algorithm as applied to the cloud top altitude and the cloud geometrical thickness determination from top-of-atmosphere reflectance measurements in the oxygen A band, Journal of Geophysical Research: Atmospheres, 109, https://doi.org/10.1029/2003JD004104, 2004.

Schlundt, C., Kokhanovsky, A. A., Rozanov, V. V., and Burrows, J. P.: Determination of cloud optical thickness over snow using satellite measurements in the oxygen A-Band, IEEE Geoscience and Remote Sensing Letters, 10, 1162–1166, https://doi.org/10.1109/LGRS.2012.2234720, 2013.

Schmale, J., Zieger, P., and Ekman, A. M.: Aerosols in current and future Arctic climate, Nature Climate Change, pp. 1–11, https://doi.org/10.1038/s41558-020-00969-5, 2021.

Schmale, J., Sharma, S., Decesari, S., Pernov, J., Massling, A., Hansson, H.-C., von Salzen, K., Skov, H., Andrews, E., Quinn, P. K., Upchurch, L. M., Eleftheriadis, K., Traversi, R., Gilardoni, S., Mazzola, M., Laing, J., and Hopke, P.: Pan-Arctic seasonal cycles and long-term trends of aerosol properties from 10 observatories, Atmospheric Chemistry and Physics, 22, 3067–3096, https://doi.org/10.5194/acp-22-3067-2022, 2022.

Schweiger, A. J.: Changes in seasonal cloud cover over the Arctic seas from satellite and surface observations, Geophysical Research Letters, 31, https://doi.org/10.1029/2004GL020067, 2004.

Screen, J. A. and Simmonds, I.: The central role of diminishing sea ice in recent Arctic temperature amplification, Nature, 464, 1334–1337, https://doi.org/10.1038/nature09051, 2010.

Serreze, M. C. and Barry, R. G.: Processes and impacts of Arctic amplification: A research synthesis, Global and Planetary Change, 77, 85–96, https://doi.org/10.1016/j.gloplacha.2011.03.004, 2011.

Serreze, M. C. and Barry, R. G.: The Arctic Climate System, Cambridge Atmospheric and Space Science Series, Cambridge University Press, 2 edn., https://doi.org/10.1017/CBO9781139583817, 2014.

Serreze, M. C. and Francis, J. A.: The Arctic amplification debate, Climatic change, 76, 241–264, https://doi.org/10.1007/s10584-005-9017-y, 2006.

Shahi, S., Abermann, J., Heinrich, G., Prinz, R., and Schöner, W.: Regional Variability and Trends of Temperature Inversions in Greenland, Journal of Climate, 33, 9391 – 9407, https://doi.org/10.1175/JCLI-D-19-0962.1, 2020.

Shupe, M. D. and Intrieri, J. M.: Cloud radiative forcing of the Arctic surface: The influence of cloud properties, surface albedo, and solar zenith angle, Journal of Climate, 17, 616–628, https://doi.org/10.1175/1520-0442(2004)017<0616:CRFOTA>2.0.CO;2, 2004.

Shupe, M. D., Rex, M., Dethloff, K., Damm, E., Fong, A. A., Gradinger, R., Heuze, C., Loose, B., Makarov, A., Maslowski, W., Nicolaus, M., Perovich, D., Rabe, B., Rinke, A., Sokolov, V., and Sommerfeld, A.: The MOSAiC Expedition: A Year Drifting with the Arctic Sea Ice, Arctic report card, https://doi.org/10.25923/9g3v-xh92, 2021.

Sledd, A. and L'Ecuyer, T.: How Much Do Clouds Mask the Impacts of Arctic Sea Ice and Snow Cover Variations? Different Perspectives from Observations and Reanalyses, Atmosphere, 10, 12, https://doi.org/10.3390/atmos10010012, 2019.

Sledd, A. and L'Ecuyer, T. S.: A Cloudier Picture of Ice-Albedo Feedback in CMIP6 Models, Frontiers in Earth Science, 9, https://doi.org/10.3389/feart.2021.769844, 2021b.

Sledd, A. and L'Ecuyer, T. S.: Emerging Trends in Arctic Solar Absorption, Geophysical Research Letters, 48, e2021GL095 813, https://doi.org/10.1029/2021GL095813, 2021a.

Smith, A., Jahn, A., and Wang, M.: Seasonal transition dates can reveal biases in Arctic sea ice simulations, The Cryosphere, 14, 2977–2997, https://doi.org/10.5194/tc-14-2977-2020, 2020.

Södergren, A. H. and McDonald, A. J.: Quantifying the Role of Atmospheric and Surface Albedo on Polar Amplification Using Satellite Observations and CMIP6 Model Output, Journal of Geophysical Research: Atmospheres, 127, e2021JD035 058, https://doi.org/10.1029/2021JD035058, e2021JD035058 2021JD035058, 2022.

Stengel, M., Mieruch, S., Jerg, M., Karlsson, K.-G., Scheirer, R., Maddux, B., Meirink, J., Poulsen, C., Siddans, R., Walther, A., and Hollmann, R.: The Clouds Climate Change Initiative: Assessment of state-of-the-art cloud property retrieval schemes applied to AVHRR heritage measurements, Remote Sensing of Environment, 162, 363 – 379, https://doi.org/10.1016/j.rse.2013.10.035, 2015.

Stengel, M., Stapelberg, S., Sus, O., Schlundt, C., Poulsen, C., Thomas, G., Christensen, M., Carbajal Henken, C., Preusker, R., Fischer, J., Devasthale, A., Willén, U., Karlsson, K.-G., McGarragh, G. R., Proud, S., Povey, A. C., Grainger, R. G., Meirink, J. F., Feofilov, A., Bennartz, R., Bojanowski, J. S., and Hollmann, R.: Cloud property datasets retrieved from AVHRR, MODIS, AATSR and MERIS in the framework of the Cloud_cci project, Earth System Science Data, 9, 881–904, https://doi.org/10.5194/essd-9-881-2017, 2017.

Stengel, M., Stapelberg, S., Sus, O., Finkensieper, S., Würzler, B., Philipp, D., Hollmann, R., Poulsen, C., Christensen, M., and McGarragh, G.: Cloud_cci Advanced Very High Resolution Radiometer post meridiem (AVHRR-PM) dataset version 3: 35-year climatology of global cloud and radiation properties, Earth System Science Data, 12, 41–60, https://doi.org/10.5194/essd-12-41-2020, 2020.

Stephens, G. L., Gabriel, P. M., and Partain, P. T.: Parameterization of Atmospheric Radiative Transfer. Part I: Validity of Simple Models, Journal of the Atmospheric Sciences, 58, 3391 – 3409, https://doi.org/10.1175/1520-0469(2001)058<3391:POARTP>2.0.CO;2, 2001.

Sus, O., Stengel, M., Stapelberg, S., McGarragh, G., Poulsen, C., Povey, A. C., Schlundt, C., Thomas, G., Christensen, M., Proud, S., Jerg, M., Grainger, R., and Hollmann, R.: The Community Cloud retrieval for CLimate (CC4CL) – Part 1: A framework applied to multiple satellite imaging sensors, Atmospheric Measurement Techniques, 11, 3373–3396, https://doi.org/10.5194/amt-11-3373-2018, 2018.

Taylor, P. C., Cai, M., Hu, A., Meehl, J., Washington, W., and Zhang, G. J.: A decomposition of feedback contributions to polar warming amplification, Journal of Climate, 26, 7023–7043, https://doi.org/10.1175/JCLI-D-12-00696.1, 2013.

Tilstra, L. G., de Graaf, M., Aben, I., and Stammes, P.: In-flight degradation correction of SCIAMACHY UV reflectances and Absorbing Aerosol Index, Journal of Geophysical Research: Atmospheres, 117, https://doi.org/10.1029/2011JD016957, 2012.

Tselioudis, G., Rossow, W. B., and Rind, D.: Global patterns of cloud optical thickness variation with temperature, Journal of climate, 5, 1484–1495, https://doi.org/10.1175/1520-0442(1992)005<1484:GPOCOT>2.0.CO;2, 1992.

Turner, J., Comiso, J. C., Marshall, G. J., Lachlan-Cope, T. A., Bracegirdle, T., Maksym, T., Meredith, M. P., Wang, Z., and Orr, A.: Non-annular atmospheric circulation change induced by stratospheric ozone depletion and its role in the recent increase of Antarctic sea ice extent, Geophysical Research Letters, 36, https://doi.org/10.1029/2009GL037524, 2009.

van Diedenhoven, B., Hasekamp, O. P., and Aben, I.: Surface pressure retrieval from SCIAMACHY measurements in the O_2 A Band: validation of the measurements and sensitivity on aerosols, Atmospheric Chemistry and Physics, 5, 2109–2120, https://doi.org/10.5194/acp-5-2109-2005, 2005.

von Savigny, C., Haley, C. S., Sioris, C. E., McDade, I. C., Llewellyn, E. J., Degenstein, D., Evans, W. F. J., Gattinger, R. L., Griffioen, E., Kyrölä, E., Lloyd, N. D., McConnell, J. C., McLinden, C. A., Mégie, G., Murtagh, D. P., Solheim, B., and Strong, K.: Stratospheric ozone profiles retrieved from limb scattered sunlight radiance spectra measured by the OSIRIS instrument on the Odin satellite, Geophysical Research Letters, 30, https://doi.org/10.1029/2002GL016401, 2003.

Walsh, J. E., Chapman, W. L., Fetterer, F., and Stewart, J. S.: Gridded Monthly Sea Ice Extent and Concentration, 1850 Onward, Version 2. Boulder, Colorado USA. NSIDC: National Snow and Ice Data Center, https://doi.org/10.7265/jj4s-tq79, accessed May 2022, 2019.

Wang, X. and Key, J. R.: Recent trends in Arctic surface, cloud, and radiation properties from space, Science, 299, 1725–1728, https://doi.org/10.1126/science.1078065, 2003.

Wang, X. and Key, J. R.: Arctic Surface, Cloud, and Radiation Properties Based on the AVHRR Polar Pathfinder Dataset. Part I: Spatial and Temporal Characteristics, Journal of Climate, 18, 2558–2574, https://doi.org/10.1175/JCLI3438.1, 2005a.

Wang, X. and Key, J. R.: Arctic Surface, Cloud, and Radiation Properties Based on the AVHRR Polar Pathfinder Dataset. Part II: Recent Trends, Journal of Climate, 18, 2575–2593, https://doi.org/10.1175/JCLI3439.1, 2005b.

Wendisch, M., Macke, A., Ehrlich, A., Lüpkes, C., Mech, M., Chechin, D., Dethloff, K., Velasco, C. B., Bozem, H., Brückner, M., Clemen, H.-C., Crewell, S., Donth, T., Dupuy, R., Ebell, K., Egerer, U., Engelmann, R., Engler, C., Eppers, O., Gehrmann, M., Gong, X., Gottschalk, M., Gourbeyre, C., Griesche, H., Hartmann, J., Hartmann, M., Heinold, B., Herber, A., Herrmann, H., Heygster, G., Hoor, P., Jafariserajehlou, S., Jäkel, E., Järvinen, E., Jourdan, O., Köstner, U., Kecorius, S., Knudsen, E. M., Köllner, F., Kretzschmar, J., Lelli, L., Leroy, D., Maturilli, M., Mei, L., Mertes, S., Mioche, G., Neuber, R., Nicolaus, M., Nomokonova, T., Notholt, J., Palm, M., van Pinxteren, M., Quaas, J., Richter, P., Ruiz-Donoso, E., Schëfer, M., Schmieder, K., Schnaiter, M., Schneider, J., Schwarzenböck, A., Seifert, P., Shupe, M. D., Siebert, H., Spreen, G., Stapf, J., Stratmann, F., Vogl, T., Welti, A., Wex, H., Wiedensohler, A., Zanatta, M., and Zeppenfeld, S.: The Arctic Cloud Puzzle: Using ACLOUD/PASCAL Multiplatform Observations to Unravel the Role of Clouds and Aerosol Particles in Arctic Amplification, Bulletin of the American Meteorological Society, 100, 841 – 871, https://doi.org/10.1175/BAMS-D-18-0072.1, 2019.

Wilks, D. S.: Resampling Hypothesis Tests for Autocorrelated Fields, Journal of Climate, 10, 65–82, https://doi.org/10.1175/1520-0442(1997)010<0065:RHTFAF>2.0.CO;2, 1997.

Wilks, D. S.: Statistical methods in the atmospheric sciences. 4th Edition., Elsevier, https://doi.org/10.1016/C2017-0-03921-6, 2020.

Zelinka, M. D., Myers, T. A., McCoy, D. T., Po-Chedley, S., Caldwell, P. M., Ceppi, P., Klein, S. A., and Taylor, K. E.: Causes of higher climate sensitivity in CMIP6 models, Geophysical Research Letters, 47, e2019GL085 782, https://doi.org/10.1029/2019GL085782, 2020.

Zheng, Y., Rosenfeld, D., and Li, Z.: Satellite inference of thermals and cloud-base updraft speeds based on retrieved surface and cloud-base temperatures, Journal of Atmospheric Sciences, 72, 2411–2428, https://doi.org/10.1175/JAS-D-14-0283.1, 2015.

Zygmuntowska, M., Mauritsen, T., Quaas, J., and Kaleschke, L.: Arctic Clouds and Surface Radiation - a critical comparison of satellite retrievals and the ERA-Interim reanalysis, Atmospheric Chemistry and Physics, 12, 6667–6677, https://doi.org/10.5194/acp-12-6667-2012, 2012.